

Discovery of a Primitive Damped Lyman α Absorber Near an X-ray Bright Galaxy Group in the Virgo Cluster¹

Todd M. Tripp,² Edward B. Jenkins,³ David V. Bowen,³ Jason X. Prochaska,⁴ Bastien Aracil,² and Rajib Ganguly⁵

ABSTRACT

We present a new ultraviolet echelle spectrum of PG1216+069, obtained with *HST*+STIS, which reveals damped Ly α (DLA) absorption as well as O I, C II, Si II, and Fe II absorption lines at $z_{\text{abs}} = 0.00632$ near the NGC4261 galaxy group in the periphery of the Virgo cluster. The absorber shows no evidence of highly-ionized gas, which places constraints on “warm-hot” missing baryons in the X-ray bright NGC4261 group. The well-developed damping wings of the Ly α line tightly constrain the H I column density; we find $\log N(\text{H I}) = 19.32 \pm 0.03$. The metallicity of this sub-DLA is remarkably low, $[\text{O}/\text{H}] = -1.60^{+0.09}_{-0.11}$, which is comparable to many analogous high-redshift systems, and the iron abundance indicates that this absorber contains little or no dust. Nitrogen is underabundant: we detect neither N I nor N II, and we show that the absence of nitrogen is not due to ionization effects but rather indicates that $[\text{N}/\text{O}] \leq -0.28$ (3σ). Despite the proximity of the sight line to NGC4261 group, there are no bright galaxies with small impact parameters at the absorption redshift: the nearest known galaxy is a sub- L^* galaxy with a projected distance $\rho = 86h_{75}^{-1}$ kpc, while the closest L^* galaxy is NGC4260 at $\rho = 246h_{75}^{-1}$ kpc. The low metallicity and nitrogen underabundance indicate that this low- z sub-DLA is a relatively primitive gas cloud. We consider the nature and origin of the sub-DLA, and we discuss several possibilities. The properties of the sub-DLA are similar to those of the interstellar media in blue compact dwarf galaxies and are also reminiscent of Milky Way HVCs. The sub-DLA could also be

¹Based on observations with (1) the NASA/ESA *Hubble Space Telescope*, obtained at the Space Telescope Science Institute, which is operated by the Association of Universities for Research in Astronomy, Inc., under NASA contract NAS 5-26555, and (2) the NASA-CNES/ESA *Far Ultraviolet Spectroscopic Explorer* mission, operated by Johns Hopkins University, supported by NASA contract NAS 5-32985.

²Department of Astronomy, University of Massachusetts, Amherst, MA 01003, Electronic mail: tripp@astro.umass.edu

³Princeton University Observatory, Peyton Hall, Princeton, NJ 08544

⁴University of California Observatories, Natural Sciences II Annex, UC-Santa Cruz, Santa Cruz, CA 95064

⁵Space Telescope Science Institute, 3700 San Martin Drive, Baltimore, MD 21218

related to a dwarf spheroidal galaxy, if the absorption arises in gas ejected or stripped from such an object. Finally, the object could simply be a small dark-matter halo, self-enriched by a small amount of internal star formation but mostly undisturbed since its initial formation. In this case, the small halo would likely be an ancient building block of galaxy formation that formed before the epoch of reionization.

Subject headings: cosmology: observations — galaxies: abundances — intergalactic medium — quasars: absorption lines — quasars: individual (PG1216+069)

1. Introduction

Understanding the metal enrichment history of the universe, in environments ranging from the low-density intergalactic medium to the highest overdensity regions in galaxies and galaxy clusters, has emerged as one of the pressing challenges of current cosmology and galaxy evolution studies. Measurements of abundances in QSO absorption line systems have shown remarkably little evolution of metallicity from $z_{\text{abs}} > 4$ down to $z_{\text{abs}} \approx 1$. Moreover, this lack of evolution is evident in all absorber samples regardless of H I column density, ranging from the low-density Ly α clouds with $N(\text{H I}) < 10^{14} \text{ cm}^{-2}$ (e.g., Songaila 2001; Pettini et al. 2003; Schaye et al. 2003; Simcoe, Sargent, & Rauch 2004) up to the highest-column density damped Ly α absorbers with $N(\text{H I}) > 10^{20} \text{ cm}^{-2}$ (e.g., Pettini et al. 1999; Prochaska & Wolfe 2002); these absorbers span several orders of magnitude in overdensity δ ($\equiv \rho / \langle \rho \rangle$). It does appear that at any particular redshift, the lower- $N(\text{H I})$ /lower- δ absorbers generally have lower overall metallicities, but it should be noted that as $N(\text{H I})$ decreases, the abundance measurements become increasingly sensitive to ionization corrections (see, e.g., Figure 13 in Schaye et al. 2003). There are also indications that absorber metallicities are highly inhomogeneous (Schaye et al. 2003), and it remains possible that some absorption systems are metal-free (e.g., Levshakov et al. 2003; Simcoe et al. 2004; Aracil et al. 2004).

For the damped Ly α absorbers (DLAs) in particular, the observation of weak evolution with redshift is intriguing. After all, the Milky Way is a damped Ly α absorber, and its ISM metallicity (in the vicinity of the Sun) is substantially higher than the DLA metallicity trend extrapolated to $z = 0$. If the DLAs arise in the bound interstellar media of objects that are the precursors of today’s spiral galaxies, which has long been the canonical view (e.g., Wolfe et al. 1986), then why are the abundances not increasing at a rate sufficient to reach solar metallicity at $z \approx 0$? Recently, Prochaska et al. (2003) have presented evidence of slowly increasing metallicity with decreasing z based on a sample of 125 DLAs, but they note that the extrapolation to $z = 0$ still falls 4σ below the Milky Way metallicity. We note, though, that the evolution of DLA metallicity with redshift still suffers from considerable uncertainty due to the limited number of robust abundance measurements in low- z DLAs (see below). Theoretical studies employing hydrodynamic simulations have reproduced the slow evolution of the DLAs but generally predict substantially higher mean metal-

licities than observed (Cen et al. 2003; Nagamine, Springel, & Hernquist 2004), a discrepancy that is attributed to either a bias in the observations due to obscured QSOs (but see counterarguments in Ellison et al. 2001; Prochaska 2003) or inadequate treatment of supernova feedback and the multiphase nature of the gas.

However, all current observational studies are dominated by absorbers with $z_{\text{abs}} \gtrsim 2$. The lookback time increases quickly with redshift, and the current samples only probe the first $\sim 20\%$ of the history of the universe. Indeed, if the DLA metallicities reported by Prochaska et al. (2003) are expressed as a function of cosmic time instead of redshift, then these latest data indicate that DLA metallicities appear to be doubling every billion years at $z \approx 3$. Without the lowest-redshift bin, extrapolation of this trend vs. time to the current epoch would predict highly super-solar abundances in DLAs at $z \approx 0$. Clearly, the lowest-redshift DLAs now present the key to understanding DLA metallicity evolution, and it is crucial to examine how the absorption systems evolve in the relatively unstudied 80% of the age of the universe between $z \approx 2$ and now. For the most part, this requires observations from space (the optimal absorption lines for abundance measurements are in the UV at these redshifts), a task which presents several challenges. Low-redshift high- $N(\text{H I})$ absorption systems are rarely found in traditionally constructed unbiased surveys; e.g., Jannuzi et al. (1998) found only one DLA in a survey of 83 QSOs with the *HST* Faint Object Spectrograph. Rao & Turnshek (2000) have demonstrated that the low- z DLA sample can be increased more rapidly by selecting targets known to show the Mg II $\lambda\lambda 2796.35, 2803.53$ doublet a priori, but even DLAs found in this way are slowly yielding metallicities, partly because the background QSOs are still too faint for follow-up high-resolution spectroscopy with current space-borne instrumentation. The lowest-redshift DLAs are especially interesting because these absorbers provide the greatest opportunity to understand the nature of the DLA progenitor. For example, we have found a DLA that originates in a low-surface brightness galaxy at $z = 0.009$ (Bowen et al. 2001a,b); this galaxy would be challenging to detect at even moderate redshifts.

For these reasons, we are pleased to report in this paper the serendipitous discovery of a new damped Ly α system at $z_{\text{abs}} = 0.00632$ in the direction of PG1216+069. Using the E140M echelle mode of the Space Telescope Imaging Spectrograph (STIS) on board *HST*, we have been conducting a large survey for low- z O VI absorption lines, which appear to harbor a significant fraction of the baryons at the present epoch (Tripp et al. 2000a,b; Savage et al. 2002; Richter et al. 2004; Sembach et al. 2004a). The sight line to one of the QSOs observed under the auspices of this O VI survey, PG1216+069, passes through a very interesting region of the nearby universe. As shown in Figure 1, this sight line pierces the southwest periphery of the Virgo galaxy cluster. The PG1216+069 sight line is outside of the 6° cluster core defined by Tully & Shaya (1984), but it is within the sphere of influence of the cluster according to those authors. An even more intriguing aspect of this sight line is that it is ~ 400 kpc in projection from the center of the NGC4261 galaxy group. This group, which is at a redshift close to (but slightly higher than) the redshift of the Virgo cluster proper, is known to have a hot intragroup medium from *ROSAT* detection of diffuse X-ray emission (Davis et al. 1995).

While observations of PG1216+069 made with the first-generation *HST* spectrographs had revealed a strong Ly α line at $z_{\text{abs}} \approx 0.006$, i.e., near the redshift of the Virgo cluster (Bowen et al. 1996; Impey, Petry, & Flint 1999), the low spectral resolution of the early *HST* spectra precluded recognition of the damped nature of this absorption system. A portion of the new STIS spectrum of this QSO covering the Ly α line in Virgo is shown in Figure 2. This Ly α line has well-developed damping wings. Technically, even though the damping wings are quite obvious, the H I column density of the $z_{\text{abs}} = 0.00632$ system is too low to qualify as a “damped” Ly α absorber according to the standard definition, which requires $\log N(\text{H I}) \geq 20.3$. Hence, we will refer to this system as a “sub-DLA”. Originally, the standard DLA definition was mainly an observational convenience for early low-resolution spectroscopic studies. In many respects, sub-DLAs can have physical characteristics that are similar to the higher $N(\text{H I})$ DLAs. However, ionization corrections can be more important in sub-DLAs (e.g., Dessauges-Zavadsky et al. 2003; Péroux et al. 2003).

In this paper we present the remarkable properties of this new, nearby sub-DLA in the immediate vicinity of the Virgo cluster. The manuscript is organized as follows: after presenting the observations and absorption line measurements in § 2 and § 3, respectively, we derive the absolute and relative metal abundances of the absorber in § 4, including analyses of potentially important sources of systematic errors such as unresolved line saturation and ionization corrections. In § 5, we briefly discuss the physical conditions in the absorbing gas. We then provide information on the environment in which the system is found (§ 6) and limits on O VI absorption associated with the NGC4261 group (§ 7) before offering some comments on the nature and implications of the absorber properties in § 8. We close with a summary of the main results in § 9, and the appendix briefly discusses STIS wavelength calibration errors.

2. Observations

PG1216+069 was observed with the E140M spectroscopic mode of STIS on 7 occasions in 2003 May-June; the total integration time was 69.8 ksec. This echelle spectrograph provides a resolution of 7 km s^{-1} (FWHM) with ~ 2 pixels per resolution element and covers the 1150–1700 Å range with only a few small gaps between orders at $\lambda > 1630 \text{ Å}$ (Woodgate et al. 1998; Kimble et al. 1998). The observations employed the $0''.2 \times 0''.06$ slit in order to minimize the wings in the line-spread function (see Figure 13.91 in the STIS Instrument Handbook, Kim Quijano et al. 2003). The data were reduced as described in Tripp et al. (2001) using the STIS Team version of CALSTIS at the Goddard Space Flight Center.

We encountered three minor calibration issues when we reduced these data. First, there are a significant number of warm/hot pixels on the detector. Some of these were successfully fixed with an automatic identification and interpolation algorithm using pixels adjacent to the hot pixels, but many of the warm pixels are not easily identified and corrected in the individual exposures due to low count rates, and these remained in the data after the hot-pixel cleaning procedure. When the individual exposures were combined into a single final spectrum, these pixels became more evident.

Fortunately, there is no clear evidence that the important absorption lines discussed in this paper are significantly affected by warm/hot pixels. Second, after flux calibration, overlapping regions of adjacent orders showed slight flux discrepancies, mainly very close to order edges. We used the recently improved ripple correction (as of 2003 July), but nevertheless these small discrepancies are likely due to residual imperfections in the ripple correction. To avoid spurious features at order edges, when we coadded the overlapping regions of adjacent orders, we smoothly decreased the weight given to the 50 pixels approaching the order edges with the last 10 pixels thrown out all together. Third, we noticed and corrected small errors ($\lesssim 1$ pixel) in the relative wavelength calibration. These wavelength calibration errors are larger than expected, and indeed are larger than we have seen in many other observations with this mode of STIS, so we have summarized the evidence of this problem in the appendix. Nevertheless, compared to archival spectra available from other UV instruments/facilities, the STIS relative wavelength calibration is still excellent, and moreover these small shifts would have very little effect on our measurements and science conclusions even if they were neglected.

PG1216+069 was also observed with the *Far Ultraviolet Spectroscopic Explorer (FUSE)* in a single visit on 2001 February 6 for 12.4 ksec (dataset root P10721).¹ This is a short exposure compared to typical *FUSE* observations of extragalactic objects, and indeed the final *FUSE* spectrum of PG1216+069 is relatively noisy. Nevertheless, we shall see that by virtue of its unique wavelength coverage, this *FUSE* spectrum provides useful constraints for our analysis of the Virgo sub-DLA. To reduce the *FUSE* data, we first calibrated the raw time-tagged data frames using the CALFUSE pipeline reduction (version 2.4.0). The calibrated datasets comprised six individual sub-exposures for each *FUSE* channel. The signal-to-noise of each subexposure was too low to permit us to derive any shifts between sub-exposures, so we simply summed the total number of counts in each pixel from all six sub-exposures. However, our experience with *FUSE* observations of substantially brighter targets indicates that shifts between sub-exposures are small or negligible in a single visit, so our procedure for coaddition of the PG1216+069 data should result in little or no degradation of spectral resolution. We binned the final coadded *FUSE* spectrum to ~ 10 km s⁻¹ pixels, which provides ~ 2 pixels per resolution element. Only the LiF channels contained enough signal to be useful, so the effective wavelength coverage of the *FUSE* spectrum is 1000-1185 Å. The usual strong ISM lines (e.g., Si II λ 1020.70, O VI $\lambda\lambda$ 1031.93,1037.62, C II λ 1036.34, Fe II λ 1144.94) are readily apparent in the final *FUSE* spectrum along with several extragalactic absorption lines. In this paper, we will make use of the *FUSE* data for two purposes. First, we will use the LiF2a segment to search for N II λ 1083.99 absorption at the redshift of the Virgo sub-DLA. Second, we will use the LiF1a and LiF2b segments to place constraints on O VI associated with the NGC4261 group and the sub-DLA. To calibrate the zero point of the LiF2a wavelength scale, we aligned the Fe II λ 1144.94 absorption profile with the profile of the Fe II λ 1608.45 line in the STIS spectrum. For the LiF1a and LiF2b spectra, we compared the C II λ 1036.34 and C II λ 1334.53 lines from

¹For information on the design and performance of *FUSE*, see §3 in Moos et al. (2002) and references therein.

the *FUSE* and STIS spectra, respectively. These Fe II and C II transitions have similar strengths,² and this procedure results in a zero-point velocity uncertainty of 5–10 km s⁻¹. Due to the low S/N ratios of the individual spectra, we aligned and coadded the LiF1a and LiF2b segments for the O VI measurements. This may degrade the spectral resolution, but examination of the coadded spectrum indicates that the degradation is minimal. In the case of the N II line, only the LiF2a spectrum had the right wavelength coverage and sufficient S/N to place useful constraints.

3. Absorption Line Measurements

A selected portion of the final, coadded STIS spectrum is shown in Figure 2. The strong Ly α absorption line at $z_{\text{abs}} = 0.00632$ is readily apparent along with adjacent lines from various redshifts including the damped Ly α line due to Galactic H I, Ly δ at $z_{\text{abs}} = 0.28228$, and Ly α at $z_{\text{abs}} = 0.00375$. The Ly δ line is recorded at low signal-to-noise ratio (S/N) due to its location in the pit of the Milky Way Ly α absorption. Nevertheless, the Ly δ identification is secure because >11 other Lyman series lines are detected at $z_{\text{abs}} = 0.28228$. Only Ly α is detected at $z_{\text{abs}} = 0.00375$. We note that Ly α absorbers are frequently detected at $0.003 \lesssim z_{\text{abs}} \lesssim 0.008$ in the spectra of QSOs in the general direction of the Virgo cluster (e.g., Bowen et al. 1996; Impey, Petry, & Flint 1999; Tripp et al. 2002; Rosenberg et al. 2003).

The well-developed Lorentzian wings of the Ly α line at $z_{\text{abs}} = 0.00632$ tightly constrain the H I column density. Since the $z_{\text{abs}} = 0.00632$ Ly α line is positioned in the red wing of the Milky Way damped Ly α profile (see Figure 2), we fitted the Milky Way H I line as well as the $z_{\text{abs}} = 0.00632$ absorber. We used the method and software described in Jenkins et al. (1999) to fit the damped Ly α profiles and measure $N(\text{H I})$.³ The resulting fit is shown with a solid line in Figure 2, and the absorber H I column densities and uncertainties are summarized in Table 1, including the weak Ly α line at $z_{\text{abs}} = 0.00375$. The H I column derived from the Milky Way Ly α profile is in good agreement with the $N(\text{H I})$ reported by Lockman & Savage (1995) based on 21cm emission in the direction of PG1216+069.

Absorption lines of O I, C II, Si II, and Fe II are detected at $z_{\text{abs}} = 0.00632$ in the STIS E140M spectrum. N I, Si IV, and C IV are not apparent at the 3σ significance level. The strong

²The Fe II and C II lines are strongly saturated and black in their cores, but since the profile edges are sharp and the lines have similar strengths and equivalent widths, the STIS and FUSE data can be aligned with good precision after the STIS resolution has been degraded to match the FUSE resolution.

³As described in Jenkins et al. (1999) and Sonneborn et al. (2000), our H I measurement software allows the height and shape of the continuum to vary during the fitting process, and the error bars reflect the continuum placement uncertainty accordingly. Inspection of the black cores of strongly saturated lines in STIS echelle spectra occasionally reveals small errors in the STIS flux zero point (usually $\lesssim 2\%$ of the continuum level). Consequently, the flux zero level was also allowed to vary as a free parameter during the fitting process, and the saturated cores of the lines were included in the χ^2 calculation.

Si III $\lambda 1206.50$ line is redshifted into the core of the Galactic Ly α line and consequently cannot be reliably measured.⁴ Selected absorption-line profiles of detected species are shown in Figure 3; non-detections are plotted in Figure 4. We have measured the rest-frame equivalent widths using the techniques of Sembach & Savage (1992), which include continuum placement uncertainty as well as a 2% uncertainty in the STIS flux zero level. These equivalent widths are listed in Table 2 along with upper limits on undetected species of interest.

We have used two techniques to estimate the column densities of metals in the sub-DLA. First, we used standard Voigt-profile fitting with the program of Fitzpatrick & Spitzer (1997) and the line-spread functions from the STIS Handbook (Kim Quijano et al. 2003). Inspection of the absorption profiles (see Figure 3) reveals two well-detected components at $v \approx 0$ and 28 km s^{-1} in the absorber velocity frame. The strongest lines show marginal evidence of additional, barely detectable components at $-125 \lesssim v \lesssim 0 \text{ km s}^{-1}$. These possible components are too poorly defined to justify any attempts to fit them with Voigt profiles. Thus, we have elected to only fit the two well-detected components; we discuss below how inclusion of the additional weak features at $v \lesssim 0 \text{ km s}^{-1}$ could affect our conclusions. Results from Voigt-profile fitting are summarized in Table 3 including the velocity centroid, b -value, and column density for the two primary components.

For our second approach, we use the more generalized technique of directly integrating the “apparent column density” profiles (see Savage & Sembach 1991; Jenkins 1996 and references therein). This method does not incorporate any assumption that the velocity profile is inherently Gaussian. Instead, each pixel is used to calculate the apparent optical depth as a function of velocity, $\tau_a(v) = \ln[I_c(v)/I(v)]$, where $I(v)$ is the observed intensity and $I_c(v)$ is the estimated continuum intensity at velocity v . In turn, $\tau_a(v)$ is used to calculate the apparent column density, $N_a(v) = (m_e c / \pi e^2) (f \lambda)^{-1} \tau_a(v)$. If the profiles do not contain narrow, saturated structures that are degraded by instrumental smoothing, then $N_a(v)$ can be directly integrated to obtain a good measurement of the total column density, $N_{\text{tot}} = \int N_a(v) dv$. As in the equivalent width measurements, we used the methods of Sembach & Savage (1992) to incorporate the uncertainties due to continuum placement and the flux zero point in the overall $N_a(v)$ error bars. The column densities from direct integration of $N_a(v)$ profiles are given in Table 2. We list both the *total* column densities (integrated across both components) and the integrated columns for the strongest component (at $v = 0 \text{ km s}^{-1}$) only. We will make use of the measurements for the strongest component only when we examine relative abundances in § 4.2.

It is important to note that several of the metal lines are strong and narrow (see Figure 3), and we should be concerned about whether unresolved saturation could cause the column densities to be underestimated. Voigt profile fitting can adequately correct for unresolved saturation to some extent by adjusting the line width, but it has been shown that when lines are significantly affected by unresolved saturation, profile fitting can produce erroneous results (e.g., Shull et al.

⁴The region of the spectrum that would encompass the Si III feature was excluded from the H I fitting discussed in the previous paragraph.

2000; Sembach et al. 2001). The apparent column density technique can also be used to check (and correct) for unresolved saturation given two or more transitions of a particular ion with significantly differing $f\lambda$ values. If the lines are not affected by saturation, then the $N_a(v)$ profiles of weaker and stronger transitions will agree. Conversely, if the profiles are affected by saturated components, then weaker transitions will yield significantly higher apparent column densities than corresponding stronger transitions.

To check for saturation in the metal lines of the sub-DLA of this paper, we made use of the fact that Si II exhibits a generous array of transitions within our spectral coverage. We detected the Si II $\lambda\lambda$ 1190.42, 1260.42, 1304.37, and 1526.71 transitions (the 1193.29 Å line could not be used due to strong blending with Galactic absorption); the weakest and strongest lines in this set differ by a factor of 12 in $f\lambda$ (see Table 2). When we compared the apparent optical depths of the different Si II lines, it was clear that they did not scale in proportion to the values of $f\lambda$, indicating the presence of unresolved saturation. A method to correct $N_a(v)$ profiles for unresolved saturation has been outlined by Jenkins (1996). The discussion in Jenkins (1996) applies to the analysis of doublets, but the arguments can be generalized to include simultaneously many lines of differing strength. We have applied this method to the sub-DLA Si II lines in order to correct for the unresolved saturation. At each velocity, we solved for the minimum values of the χ^2 in all of the recorded intensities by allowing two parameters to vary: the true column density per unit velocity $N(v)$ and a saturation parameter, one that is directly analogous to the b -value in a classical application of a curve of growth to measurements of equivalent widths. Much of the detail in the final outcome is governed by the strongest line, since it has the greatest sensitivity to small changes in $N(v)$. Nevertheless, the weaker lines are able to influence the shape of the profile where the stronger lines are affected by saturation, creating an outcome that corrects for the distortion caused by unresolved, saturated structures. This method also automatically gives the greatest weight to the most useful transition for each velocity element. That is, moderate optical depths prevail over the weak ones buried in the noise or the very strong ones that are more subject to systematic errors.

The saturation-corrected, composite Si II profile is compared to the O I λ 1302.17 and C II λ 1334.53 profiles in Figure 5. The correction implied by the Si II $N_a(v)$ profiles turned out to be relatively small, and the total Si II column derived from integration of the saturation-corrected composite Si II profile is $\log N(\text{Si II}) = 13.52$. This saturation-corrected total Si II column is in excellent agreement with the results from profile fitting (summing the two components, see Table 3), which suggests that the profile fitting properly accounts for the saturation in the case of Si II since it provides the best match to all transitions simultaneously. What about the O I and C II profiles, for which we do not have the benefit of multiple transitions for saturation checking? It is possible that the O I and especially the C II profiles are affected by unresolved saturation, but the effects of saturation are likely to be modest. We note that the shapes of the O I and C II $N_a(v)$ profiles are

in good agreement with the saturation-corrected Si II profile in the main (strongest) component.⁵ Moreover, the O I and C II b -values derived from profile fitting are in excellent agreement with the Si II b -values (see Table 3); the profile-fitting results likely correct for the saturation adequately well. Good abundances based on O I are particularly valuable, but we will show below that we reach the same essential conclusions for the abundances of the sub-DLA if we build our analysis mainly on the saturation-corrected Si II measurements, which are robust against this source of systematic error. We note that the Fe II column density from profile fitting is 0.2 dex higher than $N(\text{Fe II})$ obtained from $N_a(v)$ integration. However, the Fe II measurements are the noisiest in the set of detected lines, and in fact the Fe II columns from the two techniques agree within their 1σ uncertainties.

4. Abundances and Dust Content

We now turn to the abundances implied by the column densities contained in Tables 1-3. We begin with the absolute metallicity of the absorber (§ 4.1), and then we examine the patterns of relative abundances from element to element and explore their implications regarding the dust content and nucleosynthetic history of the sub-DLA (§ 4.2). Throughout this paper, we use the solar oxygen and carbon abundances from Allende Prieto et al. (2001,2002), and we take the N, Si, and Fe solar abundances from Holweger (2001).

4.1. Absolute Abundance

Abundance measurements in DLAs and sub-DLAs can suffer from uncertain corrections for ionization (e.g., Howk & Sembach 1999; Prochaska et al. 2002a) and depletion by dust (Prochaska 2003). It is well known that these problems can be largely avoided by using O I to determine the absolute metallicity of an absorber because (1) the ionization potentials of O I and H I are very similar, and O I is strongly tied to H I by resonant charge exchange (Field & Steigman 1971); consequently, the ionization correction is so small that it can largely be neglected for O I, and (2) evidence from the local region of our Galaxy indicates that oxygen is only lightly depleted by dust (Meyer et al. 1998; Moos et al. 2002; André et al. 2003). Our measurement of $N(\text{O I})$ is therefore particularly advantageous for constraining the metallicity of the $z_{\text{abs}} = 0.00632$ absorber. Using the summed O I column from Voigt-profile fitting for the two main components (see Table 3) and $N(\text{H I})$ from the Ly α fit, we obtain

$$[\text{O}/\text{H}] = -1.60^{+0.09}_{-0.11} \quad (1)$$

⁵Some small discrepancies are evident in the weaker component at $v \approx 25 \text{ km s}^{-1}$ in Figure 5. While these differences could be due to inadequate correction for the wavelength calibration errors noted in the appendix or could be real differences, given the weakness of this component, the disagreement could be due to noise or the possible presence of a warm pixel at the red edge of the Si II $\lambda 1260.42$ profile.

where we have used the usual logarithmic notation.⁶

There are some additional sources of uncertainty that are not incorporated into the error bar in eqn. 1. We noted in § 3 that additional weak components may be present at $v \leq 0$ km s⁻¹. These components are unlikely to be saturated by virtue of their weakness. Integrating these extra features in the O I $\lambda 1302.17$ and Si II $\lambda 1260.42$ profiles out to $v = -125$ km s⁻¹, we find that the O I column increases by 0.11 dex and $N(\text{Si II})$ increases by 0.09 dex. Therefore these extra components have only a small effect; inclusion of these components increases the metallicity by ~ 0.1 dex.

Another possible source of uncertainty in the oxygen abundance is the possibility that saturation has led to a substantial underestimate of $N(\text{O I})$. We have argued that saturation is unlikely to be a major problem (§ 3), but we can alternatively constrain the metallicity using the saturation-corrected Si II measurements. However, Si II can require significant ionization corrections (see, e.g., §5 in Tripp et al. 2003). To evaluate the ionization correction required for Si II, we have employed CLOUDY photoionization models (v94, Ferland et al. 1998) as described in Tripp et al. (2003). In these models, the gas is photoionized by the UV background from quasars at $z \approx 0$. The intensity of the UV background at 1 Rydberg is taken to be $J_\nu = 1 \times 10^{-23}$ ergs s⁻¹ cm⁻² Hz⁻¹ sr⁻¹ based on observational constraints (Weymann et al. 2001; Davé & Tripp 2001, and references therein) with the radiation field shape computed by Haardt & Madau (1996). The absorber is approximated as a constant-density, plane-parallel slab, and the thickness of the slab is adjusted to reproduce the observed H I column.

For our modeling of the ionization, we focused our attention on the main, strong component at $v = 0$; Fe II is not detected in the weaker component, and we obtain tighter constraints on N I by integrating over the stronger component only. Assuming the metallicities are similar in the strong and weak components, we reduced $N(\text{H I})$ in the strong component-only photoionization models since some of the H I is surely located in the weaker component. Based on the strong/weak component metal column density ratios, we estimate that $\log N(\text{H I}) = 19.23$ in the strong component only, and we shall see that this provides a good fit to the detected metals in this component. Figure 6 shows the column densities of O I, N I, C II, Si II, Fe II, C IV, and Si IV predicted by the photoionization model as a function of the ionization parameter U (\equiv ionizing photon density/total H number density = n_γ/n_{H}) compared to the observed column densities and upper limits (for the $v = 0$ km s⁻¹ component only). The relative metal abundances (e.g., O/Si) are fixed to the solar values according to the references at the beginning of this section and assume no depletion by dust. The model predictions are shown by solid curves with small symbols, and the observed column densities are indicated with large symbols with 1σ error bars (3σ upper limits are indicated with arrows). With the exceptions of N I and Fe II, we see that the model is in good agreement with all detections and upper limits at $\log U \approx -3.8$. The model agrees with the Fe II column from direct integration at this U as well, but $N(\text{Fe II})$ from profile-fitting is 0.2 dex higher than predicted. The Fe II line is narrow and marginally detected, and consequently this discrepancy could easily be due

⁶ $[X/Y] = \log(X/Y) - \log(X/Y)_\odot$.

to noise. We will discuss the origin of the discrepancy between the model and the observations in the case of N I below. For the assumed UV background shape and J_ν value, $\log U = -3.8$ corresponds to $\log n_{\text{H}} = -2.6$ (however, n_{H} is not well-constrained because it depends on the assumed intensity of the radiation field, which is only loosely constrained; see § 5). The absence of C IV and Si IV provide upper limits on the ionization parameter, and these upper limits translate to lower limits on the Si abundance. As U increases, $N(\text{Si II})$ predicted by the model increases (see Figure 6), so the metallicity must be decreased accordingly to match the observed Si II column. At the left edge of Figure 6, the curves each approach an asymptote for a simple reason: as U decreases, the ionization corrections become negligible, and for ions that are dominant in neutral gas, the abundance can then be calculated directly from the ion/H I ratio, e.g., $[\text{Si}/\text{H}] = [\text{Si II}/\text{H I}]$. This condition places the upper limit on $[\text{Si}/\text{H}]$. With the upper limit on U required by the Si IV constraint, we find

$$-1.77 \leq [\text{Si}/\text{H}] \leq -1.35. \quad (2)$$

The range in eqn. 2 only reflects the uncertainty in the ionization correction; the additional uncertainty due to the error bars in the column densities and solar Si abundance amounts to ± 0.08 dex. The metallicity implied by the Si II measurements is therefore similar to the absolute abundance derived from O I.

The low absolute abundances derived from the oxygen and silicon measurements are notable given the redshift of the absorber and its location in the outskirts of the Virgo cluster region and NGC4261 group (see Figure 1). As we show in Figure 7, this sub-DLA has an absolute metallicity that is similar to comparable sub-DLAs and DLAs at high redshifts. Figure 7 compares the oxygen abundance of the PG1216+069 sub-DLA (large filled circle) to the mean metallicities derived from 125 DLAs at $0.5 < z_{\text{abs}} < 5$ in six redshift bins (open squares; Prochaska et al. 2003) and individual measurements of oxygen abundances in sub-DLAs at $z_{\text{abs}} > 1.7$ (small filled circles; Dessauges-Zavadsky et al. 2003).⁷ Evidently the Virgo sub-DLA metallicity is equal to or less than the metallicity of many of the high-redshift absorbers. This suggests that this low- z absorber is a relatively primitive gas cloud.

On the other hand, the Virgo sub-DLA metallicity *is* significantly higher than the typical metallicities derived in studies of low- δ Ly α forest clouds at $z_{\text{abs}} \gtrsim 2$ (e.g., Schaye et al. 2003; Simcoe et al. 2004). This suggests that the PG1216+069 sub-DLA has somehow received at least some subsequent injection of metals above and beyond the first wave of enrichment that produced the widespread distribution of carbon and oxygen seen in the high- z forest. There are few constraints available on the metallicity of Ly α forest clouds at the present epoch. However, some low- z absorbers with H I column densities in the range expected for Ly α forest clouds have

⁷For the reasons outlined at the beginning of §4.1, we have restricted our comparison to $[\text{O}/\text{H}]$ measurements for high- z sub-DLAs, such as those from Dessauges-Zavadsky et al. (2003). In the higher- $N(\text{H I})$ DLAs, the oxygen lines are often badly saturated and/or difficult to measure due to blending with Ly α forest lines. Consequently, the DLA abundances are based on Si, S, O, or Zn measurements; see Prochaska et al. (2003) for further information.

metallicities that are considerably higher (e.g., Tripp & Savage 2000; Savage et al. 2002) than that of the Virgo sub-DLA. Therefore while the Virgo absorber is apparently not as pristine as the high- z Ly α forest, it nevertheless is relatively metal-poor compared to analogous objects in the nearby universe.

4.2. Relative Abundances and Dust

Beyond the overall metallicity, we have two motivations for scrutinizing the detailed pattern of element-to-element abundances in the sub-DLA. First, relative abundances can provide valuable constraints on the nucleosynthetic history of the object, as has been widely discussed in the stellar abundance and QSO absorption-line literature (e.g., Lauroesch et al. 1996; McWilliam 1997). Second, relative abundances can reveal the presence of dust through the patterns of differential depletion (e.g., Savage & Sembach 1996; Jenkins 2003). Unfortunately, for many elements the nucleosynthesis signatures and dust depletion patterns can be degenerate (Prochaska 2003). For this reason, nitrogen abundances are particularly valuable. Nitrogen nucleosynthesis depends on the initial metallicity of the gas, and consequently in “chemically young” gas, nitrogen is expected (and observed) to be significantly underabundant (e.g. Vila Costas & Edmunds 1993; Pettini et al. 1995; Henry et al. 2000). Nitrogen is only lightly depleted by dust (Meyer et al. 1997), so N/O provides a probe of the nucleosynthetic history that is not highly confused by dust depletion. Good iron abundances are also particularly useful because Fe is highly prone to depletion by dust, even in low-density, halo gas clouds (e.g., Savage & Sembach 1996). Consequently, iron can reveal the presence of dust when many other elements show no depletion (see further discussion in Jenkins 2003).

We begin our examination of the relative abundances with iron. We have only detected a single Fe II line, and moreover the line is weak and narrow. The Fe II column densities from direct integration and profile fitting agree to within their 1σ uncertainties, but the best values from the two techniques differ by 0.2 dex. If we neglect ionization corrections, we find $[\text{Fe}/\text{O}] = 0.15^{+0.15}_{-0.25}$ or $[\text{Fe}/\text{O}] = 0.35^{+0.15}_{-0.23}$ using the columns from direct integration and profile fitting, respectively. Dust depletion would lead to iron underabundance, but in this case the opposite trend is seen: Fe is marginally overabundant with respect to oxygen. Therefore, the iron measurements indicate that *this absorption system contains very little dust*. In principle, Fe II can also require substantial ionization corrections. However, it can be seen from Figure 6 that with the upper limit on U imposed by the high ions, the Fe II ionization correction is small. Indeed, the ionization model in Figure 6 adequately reproduces the column densities of all detections and limits (except the N I limit), without requiring any depletion, at $\log U \approx -3.8$.

Using the 3σ upper limit on $N(\text{N I})$ from Table 2 and neglecting ionization corrections, we find $[\text{N}/\text{O}] \leq -0.28$ in the strongest component of the PG1216+069 sub-DLA. While this N I underabundance could be due to ionization effects (e.g., Sofia & Jenkins 1998), the ionization model in Figure 6 shows that this is probably not due to ionization in this case if the gas is

photoionized by the background radiation from QSOs. The model in Figure 6, which assumes that the relative abundance of nitrogen to oxygen is solar, predicts a neutral nitrogen column that is ~ 0.25 dex higher than the 3σ upper limit on $N(\text{N I})$ at the best value of U . Increasing U decreases this discrepancy, but at the upper limit on U set by the absence of Si IV, the model still exceeds the 3σ upper limit (see Figure 6). We conclude that the paucity of N I reflects a true nitrogen underabundance. Our upper limit on $N(\text{N I})$ in Table 2 only assumes that the linear curve of growth is applicable; no other assumptions about the b -value were made. Figure 8 shows the predicted N I profiles for both of the main components, if we assume that the N/O ratio is solar and that the N I components have the same b -value as the detected O I components. Although the region of the strongest N I transition is close to a few warm pixels, it is nevertheless evident from Figure 8 that a solar N/O abundance does not agree with the data.

But what if the gas is also photoionized by *embedded* stars that have a much softer spectrum than the background flux employed in Figure 6? It is conceivable that the outer envelope of H I could provide enough shielding to prevent penetration of the absorber by photons with appropriate energy⁸ to produce significant amounts of Si IV and C IV, thereby satisfying the observational upper limits on these species, but lower-energy photons from internal stars could still ionize the nitrogen leading to a deficit of N I. In high-redshift DLAs, a striking correspondence between the absorption-profile structure of Al III and lower-ionization stages⁹ has been noted; this could indicate that soft stellar spectra play a role in the ionization of the high- z DLAs (e.g., Howk & Sembach 1999). Also, in the Milky Way ISM within the “Local Bubble” in the immediate vicinity of the Sun, a deficit of N I has been observed (Jenkins et al. 2000; Lehner et al. 2003); in this context, the low N I columns are quite probably due to ionization effects since other observations of sight lines extending beyond the Local Bubble boundaries suggest that the interstellar nitrogen abundance is rather uniform in the solar neighborhood, and moreover nitrogen in this region is not underabundant (e.g., Meyer et al. 1997).

Considering these observations of high- z DLAs and the Local Bubble ISM, we have multiple motivations to investigate whether ionization by light from embedded stars could be responsible for the paucity of N I in the PG1216+069 sub-DLA. The most straightforward way to test this hypothesis is to search for the N II $\lambda 1083.99$ absorption line at the sub-DLA redshift; if the lack of N I is due to ionization from soft sources, then N II should be correspondingly strong. Figure 9 shows the portion of the *FUSE* spectrum covering the N II $\lambda 1083.99$ transition at $z_{\text{abs}} = 0.00632$.

⁸High-energy photons with energies substantially greater than the ionization potentials of Si III and C III *can* penetrate a sub-DLA/DLA, but as can be seen from the model in Figure 6, which includes such photons, they are inefficient at production of Si IV and C IV.

⁹The ionization potential of Al II is 18.8 eV, so the correlation of Al III and lower-ionization stages indicates that ionized gas is present and associated with the putatively neutral gas. Unlike the Virgo sub-DLA observed toward PG1216+069, the high- z DLA and sub-DLA systems often show strong high-ion absorption from species such as Si IV and C IV, but usually the Si IV/C IV component structure is significantly different from that of the low ions and Al III (see, e.g., Lu et al. 1996; Dessauges-Zavadsky et al. 2003).

No significant N II absorption is apparent at the expected wavelength. The signal-to-noise ratio of the *FUSE* spectrum is not overwhelming, but the clear detection of absorption lines from other redshifts (see also Figure 14) demonstrates that the spectrum is adequate to reveal N II at the expected strength. Due to the lower spectral resolution of *FUSE*, the two main components of the sub-DLA are blended, so we have integrated over both components to place limits on N II. We find that $W_r \leq 140.4 \text{ m\AA}$ at the 3σ level. Assuming the linear curve-of-growth applies, this corresponds to $\log N(\text{N II}) \leq 14.07$.

What does the N II limit imply? We have computed several CLOUDY photoionization models assuming various soft ionizing radiation fields including stellar ionizing radiation approximated by a Kurucz model atmosphere with either $T_{\text{eff}} = 30,000$ or $50,000 \text{ K}$ as well as an estimate of the interstellar radiation field in the disk of the Milky Way (Black 1987). Of these three models, only the Kurucz stellar atmosphere spectrum with $T_{\text{eff}} = 50,000 \text{ K}$ satisfies the observed upper limit on N I/O I in the Virgo sub-DLA (the other two models cannot produce a low enough N I/O I ratio). However, when the N I/O I limit is satisfied, the $50,000 \text{ K}$ stellar spectrum produces an N II column density that exceeds our 3σ upper limit. Based on these models and the N II limit, we conclude that internal ionization by soft sources is also an unlikely explanation of the absence of nitrogen absorption in the PG1216+069 sub-DLA.

The finding that nitrogen is underabundant also indicates that this sub-DLA is a primitive and chemically young system. In Figure 10 we compare the Virgo sub-DLA nitrogen and oxygen abundances to measurements from a large sample of H II regions in nearby galaxies (small filled circles) and high- z DLAs (open squares). The DLA measurements in Figure 10 are from Centurión et al. (2003, and references therein) with the exceptions and additions summarized by Jenkins et al. (2004).¹⁰ The H II-region emission-line data in Figure 10 were compiled by Pilyugin et al. (2003) and converted to abundances using the “P-method”, which appears to be in better agreement with H II-region abundances with electron temperature measurements (e.g. Bresolin, Garnett, & Kennicutt 2004) than some of the more commonly used “R23” calibrations.¹¹ For comparison, figures analogous to Figure 10 but using the traditional R23 calibration can be found in Pettini et al. (2002) and Prochaska et al. (2002b). From Figure 10, we see that the N underabundance in the Virgo sub-DLA toward PG1216+069 is similar to that seen in nearby giant H II regions and distant DLAs, but the absolute metallicity of the sub-DLA is lower than the metallicities of the vast majority of the nearby galaxies.

¹⁰Jenkins et al. (2004) have carefully screened the high- z DLA data, particularly to check for abundance estimates that may be underestimated due to saturation, and substituted unsaturated α - element abundances when available.

¹¹See Kobulnicky & Kewley (2004) for a detailed discussion and comparison of R23 calibrations from the literature. Kobulnicky & Kewley note that the P-method might not be well-calibrated in the high-metallicity regime, but this does not affect the main conclusions that we draw from Figure 10 because the most relevant comparison is to the low-metallicity H II region measurements. Use of other R23 calibrations would increase the α abundances by a few tenths of a dex for the higher-metallicity H II regions.

For the most part, the second (weaker) component at $v = 28 \text{ km s}^{-1}$ offers fewer constraints and noisier measurements. We note that the column density ratios agree in both components to within the measurement uncertainties. The C II column density, however, is more reliably measured in the weaker component [$N(\text{C II})$ is uncertain in the stronger component due to saturation], and the carbon and oxygen columns indicate that $[\text{C/O}] \approx 0$ if ionization corrections are neglected. This is somewhat surprising because observations of metal-poor Galactic halo stars by Akerman et al. (2004) indicate that $[\text{C/O}] \approx -0.5$ when $[\text{O/H}] \lesssim -1$ (see their Figure 5). Akerman et al. also report a tentative indication that $[\text{C/O}]$ may return to near-solar values in the lowest-metallicity stars. The weaker component of the PG1216+069 sub-DLA may therefore have an abundance pattern more similar to the most metal-poor stars in the Akerman sample. However, $[\text{C/O}]$ in the sub-DLA is sensitive to ionization corrections (note how the C/O ratio changes as U increases in Figure 6). The uncertain ionization correction and measurement uncertainties of the current data allow a substantially lower value of $[\text{C/O}]$ in the PG1216+069 sub-DLA.

4.3. Molecular Hydrogen

We have investigated whether or not absorption features from molecular hydrogen can be seen in the FUSE spectrum of PG1216+069 at the sub-DLA redshift. Under the most probable conditions for rotational excitation ($50 \lesssim T_{\text{rot}} \lesssim 1000 \text{ K}$), we expect the strongest H_2 features to be those from the $J = 1$ level. At the positions of three strong transitions from this level, the Werner 0–0 R(1) and Q(1) lines plus the Lyman 7–0 R(1) line, we measured an average for the equivalent widths equal to $W_r = 40 \text{ m}\text{\AA}$ with a 1σ uncertainty of $30 \text{ m}\text{\AA}$, which does not constitute a real detection. We may derive a 3σ upper limit for $N(\text{H}_2)$ in the $J = 1$ level by evaluating the column density on the damping part of the curve of growth for $W_r = 130 \text{ m}\text{\AA}$ for any of the three lines, all of which have nearly the same wavelengths, f -values (Abgrall & Roueff 1989) and lifetimes (Morton & Dinerstein 1976). Our upper limit is $N(\text{H}_2) = 7 \times 10^{17} \text{ cm}^{-2}$ in the $J = 1$ level. If we assume the maximum H_2 rotational temperature observed in the Milky Way, $T_{\text{rot}} \approx 1000 \text{ K}$, then the upper limit on H_2 in all rotational levels is roughly $3 \times N(\text{H}_2, J = 1)$ (Jenkins et al. 2004 and references therein). Therefore our upper limit for the fraction of hydrogen atoms in molecular form $f(\text{H}_2) \equiv 2N(\text{H}_2)/[2N(\text{H}_2) + N(\text{H I})] < 0.17$. This limit is above values found for high- z DLAs (Curran et al. 2004 and references therein) and the Magellanic Clouds (Tumlinson et al. 2002), but is below measurements toward some moderately reddened stars in our Galaxy (Savage et al. 1977). However, when the H I column density of the PG1216+069 sub-DLA is taken into account, we see from Figure 8 in Tumlinson et al. (2002) that a rather low $f(\text{H}_2)$ value would be expected even in Milky Way sight lines. Also, since H_2 forms primarily on the surface of dust grains, a low H_2 fraction is expected in the Virgo sub-DLA given the low metallicity and dust content derived in the previous sections.

5. Physical Conditions and Neutral Gas Content

In addition to abundance constraints, the ionization models provide information on physical conditions of the gas such as the particle number density, temperature, thermal pressure, and neutral fraction of the gas. The gas ion fractions and therefore the neutral gas content of the absorber are generally well-constrained by the models. Other physical quantities suffer greater uncertainties. For example, in principle n_{H} is directly related to the ionization parameter U , but there is a caveat: since $U = n_{\gamma}/n_{\text{H}}$, the derived n_{H} depends on the intensity taken for the ionizing radiation field. For the model shown in Figure 6, we have assumed $J_{\nu} = 10^{-23}$ ergs cm $^{-2}$ s $^{-1}$ Hz $^{-1}$ sr $^{-1}$, a value in good agreement with current observational bounds on the UV background from QSOs at $z \approx 0$. However, J_{ν} is still only loosely bracketed by observations (see, e.g., Shull et al. 1999; Davé & Tripp 2001; Weymann et al. 2001). Moreover, given the high $N(\text{H I})$ of the PG1216+069 sub-DLA, it is possible that stars are located in or near the gas. We have constructed photoionization models for the Virgo sub-DLA assuming that nearby hot stars contribute to the ionizing radiation in addition to the flux from background quasars, and we reach generally similar conclusions regarding the ionization corrections and neutral gas fraction based on the stars+QSOs model. However, adding stars increases n_{γ} , and therefore a stars+QSOs model at the same value of U has to have a higher n_{H} than the analogous QSOs-only model. For this reason, the n_{H} constraints from the QSOs-only model are most conservatively treated as *lower limits*. In turn, the implied gas pressure is also a lower limit, and the line-of-sight absorber size is an upper limit. The mean gas temperature also depends on the model parameters, but less sensitively.

With this caveat, we show in Figures 6 and 11 some of the physical conditions implied by the photoionization modeling. The top axis of Figure 6 shows the particle density for the QSOs-only ionizing radiation field for the assumed value of J_{ν} at 1Ryd; we treat these densities as lower limits. Figure 11 presents the H I ion fraction (left axis) and mean gas temperature (right axis) for the same model as a function of $\log U$. The upper limit on $N(\text{Si IV})$ requires $\log n_{\text{H}} \geq -3.4$, $\log f(\text{H I}) \geq -0.9$, $T \leq 14,000$ K, and thermal pressure $P/k \geq 10$ K cm $^{-3}$. In this model, the line-of-sight absorber size is less than ~ 100 kpc. We see from Figure 11 that even though high ions such as Si IV and C IV are not detected in the Virgo sub-DLA, it could still contain a substantial amount of ionized gas. At the best-fitting ionization parameter ($\log U \approx -3.8$, shown with a thick vertical line in Figure 11), $\sim 60\%$ of the hydrogen is ionized. While the particle number density and absorber size are uncertain, it is interesting to note that the gas could be self-gravitating with the physical conditions indicated by the model in Figure 6 at $\log U \approx -3.8$, assuming the baryon-to-dark matter ratio $\Omega_b/\Omega_m \approx 0.15$ (see, e.g., Schaye 2001). Other confinement options (e.g., pressure confinement) remain viable, but gravitational confinement is not ruled out.

6. Absorber Environment

As noted in §1 and shown in Figure 1, the sight line to PG1216+069 pierces the outskirts of the Virgo cluster and the X-ray bright NGC4261 galaxy group (Davis et al. 1995). Although the sight line does not penetrate the Virgo cluster 6° core, it does pass within the cluster’s maximum angle of influence according to the model of Tully & Shaya (1984). The QSO is also in the general direction of the Virgo W and W’ structures south of the cluster proper (e.g., de Vaucouleurs 1961; Binggeli et al. 1993). Compared to most low- z Ly α absorbers, the PG1216+069 sub-DLA is certainly located in a region of relatively high galaxy density. To show this, we plot in Figure 12 the number of galaxies from the RC3 catalog (de Vaucouleurs et al. 1991) within projected distances of $3h_{75}^{-1}$ Mpc and $300h_{75}^{-1}$ kpc from the PG1216+069 sight line. Comparing Figure 12 to the analogous figures in Bowen, Pettini, & Blades (2002), we see that on the 3 Mpc scale, the galaxy density is substantially larger than the galaxy density in the vicinity of a typical low- z Ly α cloud. From Figure 12 we see that the PG1216+069 sub-DLA is at a somewhat higher velocity than the bulk of the galaxies in the Virgo cluster proper; the sub-DLA is closer in velocity to the Virgo W structure.

Given the high $N(\text{H I})$ of the absorber, some models would predict that the absorption arises in the bound ISM of a Virgo galaxy, which one might expect to find near the sight line. However, the nearest L^* galaxy near $z \sim 0.00632$ is NGC4260 (Bowen et al. 1996; Impey et al. 1999), which has a surprisingly large impact parameter ρ of $246 h_{75}^{-1}$ kpc. As noted by Impey et al. (1999), VCC297 is also near the sub-DLA redshift and has a smaller projected distance, $\rho = 86h_{75}^{-1}$ kpc. The luminosity of VCC297 is less than $0.25L^*$. NGC4260 is, in fact, the nearest galaxy to the PG1216+069 sight line that Davis et al. (1995) identify within the diffuse X-ray emitting gas in the NGC4261 group. The RC3 redshift of NGC4260 is $1886 \pm 61 \text{ km s}^{-1}$, which is the same as the sub-DLA redshift within the 1σ uncertainty. The redshifts of the other galaxies in this group listed by Davis et al. range from 2210 km s^{-1} (NGC4261) to 2685 km s^{-1} (NGC4281), i.e., within $300\text{-}800 \text{ km s}^{-1}$ of the absorber redshift. NGC4261 is a giant elliptical galaxy located near the peak of the X-ray emission; this is likely the center of mass of the group. If the PG1216+069 sub-DLA is within the NGC4261 group and the redshift of NGC4261 reflects the group distance, then the absorber impact parameter to the group $\sim 400 h_{75}^{-1}$ kpc.

Chen et al. (2001) have obtained high-resolution *HST*/WFPC2 imaging and spectroscopic galaxy redshifts in order to study the relationship between the galaxies and Ly α clouds in the direction of PG1216+069, and they have not found any close galaxies at Virgo redshifts either. Figure 13 shows a portion of a WFPC2 image of the QSO with the redshifts from Chen et al. labeled. While a number of galaxies with unknown redshifts are readily apparent in Figure 13, based on their angular sizes, these galaxies are likely to be distant background galaxies beyond Virgo. The galaxies with unknown redshifts are also quite faint; apart from the extended spiral at $z = 0.1242$, most of the galaxies near the sight line in Figure 13 have $m \gg 21$ in the WFPC2 F702W filter. We note that a bright foreground star is present near PG1216+069, and while unlikely, a Virgo galaxy could be masked by this foreground object.

7. Warm-Hot Gas in the NGC4261 Galaxy Group

The proximity of the sight line to the X-ray bright NGC4261 group provides an opportunity to test ideas regarding the location of the “missing baryons” at the present epoch. As has been widely discussed by various authors (e.g., Persic & Salucci 1992; Fukugita, Hogan, & Peebles 1998) the combined masses in well-observed baryonic components of the nearby universe do not add up to the expected mass in baryons predicted by D/H measurements and cosmic microwave background observations (e.g., Spergel et al. 2003; Sembach et al. 2004b), the so-called missing-baryons problem. Hydrodynamic simulations of cosmological structure evolution suggest that these missing baryons are located in “warm-hot” shock-heated gas at $10^5 - 10^7$ K in regions of the intergalactic medium at modest overdensities (e.g., Cen & Ostriker et al. 1999; Davé et al. 2001). In contrast, Fukugita et al. (1998) have hypothesized that the missing baryons are predominantly found in similarly-hot gas, but in higher overdensity regions near galaxy groups. In either case, the O VI doublet provides a sensitive means to search for the warm-hot gas since the O VI ion fraction peaks at $T \sim 10^{5.5}$ K. Observations of low- z QSOs have frequently revealed redshifted O VI absorption lines that are clearly correlated with galaxies (e.g., Tripp & Savage 2000; Chen & Prochaska 2000; Tripp et al. 2001; Savage et al. 2002; Sembach et al. 2004a), but so far these studies have not had sufficient information regarding the nearby galaxies to establish if they form a bound group with the overdensity expected in the Fukugita et al. hypothesis or if they are situated in lower overdensity unvirialized environments as expected from the cosmological simulations.

A few preliminary searches for O VI associated with well-defined galaxy groups have been attempted (e.g., Wakker et al. 2003; Pisano et al. 2004), but no definitive detections of O VI have yet been reported. The PG1216+069 sight line through the NGC4261 group is appealing for this purpose because the diffuse X-ray emission establishes that the group certainly contains intragroup gas, at least in its inner regions, and because the sight line impact parameter is relatively small (compared to available QSO/group pairs bright enough for high-resolution UV spectroscopy with current facilities). Figure 14 shows the portion of the *FUSE* spectrum of PG1216+069 covering the O VI doublet at the redshifts of the NGC4261 group (the expected wavelengths of O VI at the redshift of the sub-DLA are also marked). No O VI absorption is evident at the NGC4261 or sub-DLA redshifts. Unfortunately, the stronger O VI $\lambda 1031.93$ line falls in a messy region affected by the Galactic O I $\lambda 1039.23$ absorption, a Ly β line at $z_{\text{abs}} = 0.01258$, and terrestrial O I airglow emission lines (Feldman et al. 2001).¹² Consequently, we must rely on the weaker line to place upper limits on the O VI column density. Integrating over the velocity range of the detected low-ionization lines in the sub-DLA, we obtain a 3σ upper limit of $\log N(\text{O VI}) \leq 14.26$; limits at the slightly higher redshift of the NGC4261 group are similar assuming a comparable velocity integration range.

This constraint is limited by the modest signal-to-noise ratio of the data. Nevertheless, the

¹²Based on the strength of the O I $\lambda 1302.17$ transition in the STIS spectrum, O I $\lambda 1039.23$ should be detectable in the *FUSE* data. Evidently the 1039.23 line is largely filled in by terrestrial O I $\lambda 1039.23$ emission.

upper limit is comparable to the column densities of the stronger O VI absorbers detected in other directions (e.g., Tripp et al. 2000a; Chen & Prochaska 2000; Savage et al. 2002; Howk, Prochaska, & Chen 2004). Given the detection of X-ray emitting gas with ROSAT (Davis et al. 1995), it seems possible that the intragroup gas is too hot to show O VI (i.e., the oxygen is predominantly in higher ionization stages). However, in this case the sub-DLA might be expected to show, e.g., C IV from the interface between the hot X-ray gas and the low-ionization gas.

8. Discussion

The absorber properties derived above for the PG1216+069 sub-DLA are, in some regards, surprising. The gas metallicity is extremely low given the location of the gas in a region of relatively high galaxy density near the Virgo cluster and an X-ray bright galaxy group. In fact, the absolute abundance of this sub-DLA is comparable to the lowest *gas-phase* metallicities known in the nearby universe (see Figure 10). For example, the blue compact dwarf (BCD) galaxies I Zw 18 and SBS0335-052 are among the most metal-poor galaxies so far found at low redshifts. Analysis of H II region emission lines indicates that these BCD galaxies have gas-phase metallicities $Z \approx 0.02Z_{\odot}$ (Izotov et al. 1999). Measurement of absorption lines in I Zw 18 yield similar low metallicities; possibly the abundances in the diffuse H I regions probed by the absorption lines are a few tenths of a dex lower than the H II region abundances (Aloisi et al. 2003; Lecavelier des Etangs et al. 2004). Even lower metallicities have been observed in high- z QSO absorption systems and some Galactic stars, but high- z absorbers and low-metallicity stars both probe earlier epochs in the history of the universe; the DLA discussed in this paper provides information about the *current* metallicity of the absorbing entity.

But what is the nature of the absorbing entity? The absorber has similarities to some well-studied low- z objects. The PG1216+069 sub-DLA is reminiscent of the BCD galaxy I Zw 18 in many ways. As already noted, both objects have extremely low gas-phase metallicities. Like the PG1216+069 sub-DLA, I Zw 18 contains a lot of neutral gas (van Zee et al. 1998b; Aloisi et al. 2003; Lecavelier des Etangs et al. 2004). However, the most intriguing similarities of the sub-DLA and the BCD galaxy are the relative metal abundances. Aloisi et al. (2003) find that nitrogen is highly underabundant in I Zw 18, and yet they find no clear indication of α -element overabundances. On the contrary, they report that the α -elements O and Si are marginally *underabundant* with respect to iron. The abundance pattern in I Zw 18 is apparently similar to the abundance pattern that we find in the Virgo sub-DLA (see § 4). The apparent lack of an identified counterpart for the PG1216+069 sub-DLA could be used to argue against the hypothesis that the sub-DLA is somehow related to a BCD galaxy. One might expect to see evidence of a I Zw 18-like galaxy in the image shown in Figure 13. However, the QSO itself as well as the bright foreground star could mask a faint galaxy close to the sight line.

The high-velocity clouds (HVCs) in the vicinity of the Milky Way are also similar to the PG1216+069 sub-DLA in several respects. The HVCs have comparable H I column densities

(Wakker & van Woerden 1997; Wakker 2001), and when HVC metallicities have been measured, they have showed similar abundance patterns. For example, HVC Complex C has a sub-solar absolute abundance, $[O/H] \approx -0.8$, it shows a significant nitrogen underabundance, and Complex C iron abundances indicate that there is little or no dust depletion (Murphy et al. 2000; Richter et al. 2001; Gibson et al. 2001; Collins et al. 2003; Tripp et al. 2003; Sembach et al. 2004b). In all of these respects, the PG1216+069 Virgo sub-DLA is analogous to Complex C, although the sub-DLA has a substantially lower overall metallicity than Complex C. Some redshifted gas clouds analogous to the Milky Way HVCs have been detected in 21 cm emission studies, e.g., the Leo ring in the M96 group (Schneider 1989) or the large H I cloud near 3C 273 (Giovanelli & Haynes 1989). Usually these 21 cm clouds have been shown to be closely associated with some type of galaxy, albeit faint in some cases (e.g., Salzer et al. 1991).

It is worth noting that a lack of α -element enhancement (with respect to Fe) at low absolute metallicity has been also observed in stars in several nearby dwarf spheroidal (dSph) galaxies (Shetrone, Côté, & Sargent 2001; Tolstoy et al. 2003). Dwarf spheroidal galaxies generally have only small amounts of associated neutral interstellar gas, at least in the main galaxy where the stars are found (e.g., Carignan 1999). Nevertheless, there may be a connection between high- $N(\text{H I})$ absorbers and dSph's. Consider the Sculptor dSph galaxy. In this galaxy, 21cm observations show little emission centered on the stars in the galaxy, but two lobes of 21cm emission are detected at offsets of 15 – 20' from the optical (stellar) galaxy (Carignan et al. 1998). The symmetric morphology of the 21cm emission is suggestive of a bipolar outflow. Removal of interstellar gas from dSph's, either by supernovae-driven winds or by dynamical processes (tidal or ram-pressure stripping), would help to explain the paradoxical indications of extended periods of star-formation in dSph galaxies, which is difficult to reconcile with their current lack of interstellar gas (Blitz & Robishaw 2000; Grebel, Gallagher, & Harbeck 2003). Once the gas has been removed from the dSph galaxy, it could then give rise to a DLA. If a QSO sight line happened to pass through one of the 21cm emission lobes near Sculptor, for example, the resulting absorber properties would likely be very similar to the PG1216+069 sub-DLA.

Bowen et al. (1997) have searched for absorption lines in the vicinity of the dSph galaxy Leo I using three background QSOs/AGNs at projected distances ranging from 2-8 kpc. One of their spectra has insufficient signal-to-noise to place interesting limits, but the spectra of the other two QSOs show no absorption at the velocity of Leo I, and Bowen et al. argue that $N(\text{H I}) \lesssim 10^{17} \text{ cm}^{-2}$ within 2-4 kpc of that dSph. Leo I therefore presents an interesting contrast to the Sculptor dSph, and the Bowen et al. study argues against the hypothesis that dSph's are a source of high- $N(\text{H I})$ absorption systems. There are various possible explanations for the differences between Sculptor, which shows high- $N(\text{H I})$ in its immediate vicinity, and Leo I, which apparently does not. Sculptor is one of the nearest of the satellite galaxies of the Milky Way; Leo I is at least twice as far away. Perhaps gas is only stripped when the dSph's pass close to the Milky Way (Blitz & Robishaw 2000; Grebel et al. 2003) and then dissipates relatively quickly (see Bowen et al. 1997). However, there are no known luminous, large galaxies near the PG1216+069 sight line, so if this

is the correct explanation for the difference between Sculptor and Leo I, it then seems unlikely that the PG1216+069 sub-DLA is related to a dSph. Another possibility is that Sculptor and its associated clouds are related to the Magellanic Stream, which is located in the Sculptor direction and has similar velocities (Putman et al. 2003).

A final possibility is that the PG1216+069 sub-DLA arises in a small, ancient dark-matter minihalo that formed before the epoch of reionization and subsequently evolved largely undisturbed. Abel & Mo (1998) have argued that minihalos formed before reionization could accumulate and retain substantial quantities of H I, and moreover their densities would likely be high enough so that the objects would remain neutral after the substantial increase in background UV flux at the reionization epoch. Minihalos formed after reionization would, in contrast, be more highly ionized, hotter, and less able to accrete and retain gas (e.g., Bullock, Kravtsov, & Weinberg 2000). Maller et al. (2003) have recently revisited this idea, and they conclude that while minihalos are unlikely to give rise to Lyman limit absorbers, they could be a significant source of sub-DLA systems.

The simple kinematical structure of the PG1216+069 sub-DLA is consistent with expectations for minihalos, which would have circular velocities $v_c \lesssim 30 \text{ km s}^{-1}$. Kepner et al. (1999) have modeled the absorption-line signatures of photoionized gas in dark-matter minihalos, and their column density predictions, including the H I column density, the upper limit on molecular hydrogen, and the low ion/high ion column density ratios of the metals, are consistent with the observed properties of the Virgo sub-DLA if the sight line intercepts the minihalo at $\rho \sim 1 \text{ kpc}$ (see Figures 2 and 5 in Kepner et al). Bearing in mind the caveats of § 5, it is interesting to note that the line-of-sight thickness of the best-fitting CLOUDY model shown in Figure 6 would be consistent with the size implied by the Kepner et al. model if $\log U \lesssim -4.0$. Given that there could be some starlight that contributes to the ionizing flux (which makes the absorber thickness smaller), the Kepner et al. size can be reconciled with the photoionization models for the PG1216+069 sub-DLA. The sub-DLA metallicity is larger than metallicities typically derived for diffuse Ly α forest gas at high redshifts, so this hypothesis would require some self-enrichment from internal stars in the minihalo. Very low-level star formation and self enrichment are plausible, e.g., triggered by occasional perturbations of the gas, but one weakness of this idea is that a small number of supernovae could blow away the gas in the minihalo.

9. Summary

Using a new high-resolution observation of PG1216+069 obtained with the E140M echelle mode of STIS, we have identified a nearby sub-damped Ly α absorber at $z_{\text{abs}} = 0.00632$ with $\log N(\text{H I}) = 19.32 \pm 0.03$. This absorption system has several remarkable properties. First, the overall metal abundance is surprisingly low; we find $[\text{O}/\text{H}] = -1.60^{+0.09}_{-0.11}$ and $-1.77 \leq [\text{Si}/\text{H}] \leq -1.35$. These are among the lowest metallicity measurements *in the gas phase* known in the nearby universe (stars can have much lower abundances, but low stellar abundances are fossils that mainly provide information about earlier epochs). Second, the iron abundance indicates that this absorber harbors very little

dust. Third, nitrogen is significantly underabundant, which indicates that the gas is “chemically young”. However, comparison of the oxygen, silicon, and iron abundances shows no significant evidence of α -element overabundances. Fourth, although the gas is situated in the outer reaches of the Virgo galaxy cluster and the NGC4261 galaxy group, there are no known luminous galaxies within the projected distance that might be expected for such a high- $N(\text{H I})$ absorber. The nearest L^* galaxy is NGC4260 at a projected distance of $246 h_{75}^{-1}$ kpc, and even the closest known sub-luminous galaxy is at a substantial projected distance, $\rho = 86 h_{75}^{-1}$ kpc. We place limits on O VI absorption associated with the NGC4261 galaxy group, which is known to have hot intragroup gas from detection for diffuse X-ray emission.

The abundance patterns in the sub-DLA are reminiscent of abundances in nearby dwarf galaxies and of gas-phase abundances in high-velocity clouds near the Milky Way. We discuss the possibility that this absorber is related to a dwarf galaxy and/or a high-velocity cloud in the outer region of the Virgo galaxy cluster. It is also possible that the PG1216+069 sub-DLA arises in a small dark-matter halo. In this case, it is likely that the halo formed and accumulated gas in the early universe before reionization occurred, and since that time has only undergone meager self-enrichment from internal star formation. Several future measurements would be helpful for understanding the nature of this absorber. Better measurements of the Fe abundance would be valuable for learning about relative abundance patterns in the sub-DLA; in addition, the strong Fe II lines and higher signal-to-noise achievable with the far-UV mode of STIS would enable detection of weaker absorption components. We have shown that weak components will not affect the derived total abundances much, but the *kinematics* implied by the presence (or absence) of higher velocity features would be useful for testing the small dark-matter halo interpretation. A minihalo should have a low circular velocity and simple kinematics, and high-velocity weak components are not expected in this model. A deep 21 cm emission map with high spatial resolution at Virgo redshifts would test several of the possible interpretations we have presented for the sub-DLA. For example, if the sub-DLA is part of a tidally-stripped gas structure or is analogous to the H I ring in the M96 group or the Giovanelli & Haynes cloud, this would be revealed by deep 21 cm observations. Moreover, such structures would have clearly different morphologies from a minihalo or compact high-velocity cloud. Narrow-band $\text{H}\alpha$ imaging could also provide useful clues about the nature of the sub-DLA, e.g., to search for evidence of a faint star-forming galaxy near the sight line. Regardless of the detailed nature of the absorber, this observation unambiguously shows that relatively primitive gas that has undergone little chemical enrichment (compared to metallicities in high-redshift gases) is still found at the present epoch.

This paper benefitted from valuable discussions with Ari Maller, Max Pettini, Blair Savage, Ken Sembach, and Jason Tumlinson. We also appreciate useful comments from the referee. The STIS observations were obtained under the auspices of *HST* program 9184, with financial support through NASA grant HST-GO-9184.08-A from the Space Telescope Science Institute. We also appreciate and acknowledge support from NASA LTSA grant NNG04GG73G. The *FUSE* data were obtained by the PI team of the NASA-CNES-CSA *FUSE* project, which is operated by Johns

Hopkins University with financial support through NASA contract NAS 5-32985. This research has made use of the NASA/IPAC Extragalactic Database (NED), which is operated by the Jet Propulsion Laboratory, California Institute of Technology, under contract with NASA.

A. STIS Wavelength Calibration Errors

According to the Cycle 13 STIS Handbook, the relative wavelength calibration of STIS spectra recorded with the MAMA detectors is accurate to 0.25-0.5 pixels across an exposure, and the absolute wavelength calibration (i.e., the zero point) is good to 0.5–1.0 pixels (Kim Quijano et al. 2003). We have examined many spectra obtained with the STIS echelle modes (which use the MAMA detectors), and in general we have found the wavelength calibration to be excellent. Jenkins & Tripp (2001) noticed small wavelength calibration errors in a particular order of a set of E230H spectra, but in various projects using STIS E140M spectra of a large number of targets, we have usually found that absorption lines (that are appropriate for comparison) are well-aligned across the full wavelength range of STIS echelle spectra, in agreement with the accuracies reported in the STIS Handbook. Consequently, we were surprised to find evidence of somewhat larger wavelength calibration errors in the STIS E140M echelle spectrum of PG1216+069. We find indications that the relative wavelength calibration errors are as large as ~ 1 pixel. Some of this evidence is shown in Figures 15-17. Figures 15 and 16 compare $N_a(v)$ profiles of several of the absorption lines in the $z_{\text{abs}} = 0.00632$ absorption system. In the left panels in these figures, no shifts have been applied to the wavelength scale in the final reduced spectrum. Differences in the velocity centroids of these lines are readily apparent. In the right panels in Figures 15-16, shifts of ~ 1 pixel have been applied to several of the lines, as described in the captions. Clearly, the ~ 1 pixel corrections improve the alignment of the various lines observed in this absorber. In this paper, we have shifted lines at $\lambda_{\text{ob}} < 1200 \text{ \AA}$ and $\lambda_{\text{ob}} > 1330 \text{ \AA}$ by $+3.5 \text{ km s}^{-1}$.

Do we expect the transitions in Figures 15-16 to be well aligned? Could some multiphase/multicomponent aspect of the absorber cause real differences in the kinematics of the various species compared in these figures? The Si II transitions in Figure 16 should all show the same kinematical behavior. Multiple components that are blended and unresolved could lead to confusing line profile differences in comparisons of strong and weak transitions of a particular species (because column density components can be detectable in the strong lines but not the weak ones). However, comparisons of the weaker Si II transitions (e.g., 1304.37 vs. 1526.71) as well as weak vs. strong transitions (e.g., 1260.42 and 1526.71) consistently require the same shifts, which suggests that this not a component structure effect. Moreover, several other line comparisons consistently indicate that the same wavelength scale corrections are needed. We find that lines at $\lambda > 1330 \text{ \AA}$ and $\lambda < 1200 \text{ \AA}$ must be shifted compared to lines within the 1200-1330 \AA range. For example, Figure 15 shows several species that are the dominant ionization stage in H I regions; these lines require the same shifts seen in the Si II lines in Figure 16. In principle, dominant ions such as C II, Si II, and Fe II could arise in ionized gas as well as the neutral gas, and this could cause profile differences, but the fact that

the same shifts are indicated by the data in Figure 15 argues that this is not an ionization effect. Similarly, Figure 17 overplots the Milky Way S II $\lambda 1259.52$ and Fe II $\lambda 1608.45$ $N_a(v)$ profiles, and the same shift leads to significantly improved alignment of these Galactic lines. The S II and Fe II lines in Figure 17 are expected to have very similar strengths based on the abundances of these species in the ISM and their atomic data, and these lines are expected to be well-aligned. In this case, greater depletion of Fe by dust might generate profile differences, but since the same velocity shift is again mandated, we believe that the difference in the left panel of Figure 17 is more likely due to wavelength calibration errors.

We have also reduced the PG1216+069 E140M spectrum using the STScI pipeline, and we find that the final pipeline spectrum is very similar to our spectrum (which was reduced with the STIS Team software) and shows the same evidence of wavelength scale errors. We conclude that the PG1216+069 spectrum shows unusually large relative wavelength errors compared to most STIS echelle spectra that we have studied. However, even with these larger errors, the wavelength calibration is still very good compared to most archival UV spectra obtained with other *HST* instruments and other space-borne UV facilities.

REFERENCES

- Abel, T., & Mo, H. J. 1998, *ApJ*, 494, L151
- Abgrall, H. & Roueff, E. 1989, *A&AS*, 79, 313
- Akerman, C. J., Carigi, L., Nissen, P. E., Pettini, M., & Asplund, M. 2004, *A&A*, 414, 931
- Allende Prieto, C., Lambert, D. L., & Asplund, A. 2001, *ApJ*, 556, L63
- Allende Prieto, C., Lambert, D. L., & Asplund, A. 2002, *ApJ*, 573, L137
- Aloisi, A., Savaglio, S., Heckman, T. M., Hoopes, C. G., Leitherer, C., & Sembach, K. R. 2003, *ApJ*, 595, 760
- André, M. K., et al. 2003, *ApJ*, 591, 1000
- Aracil, B., Petitjean, P., Pichon, C., & Bergeron, J. 2004, *A&A*, 419, 811
- Binggeli, B., Popescu, C. C., & Tammann, G. A. 1993, *A&AS*, 98, 275
- Black, J. H. 1987, in *Interstellar Processes*, eds. D. J. Hollenbach & H. A. Thronson, (Dordrecht: Reidel), 731
- Blitz, L., & Robishaw, T. 2000, *ApJ*, 358, 375
- Böhringer, H., Briel, U. G., Schwarz, R. A., Voges, W., Hartner, G., & Trümper, J. 1994, *Nature*, 368, 828
- Bowen, D. V., Blades, J. C., Pettini, M. 1996, *ApJ*, 464, 141
- Bowen, D. V., Huchtmeier, W., Brinks, E., Tripp, T. M., & Jenkins, E. B. 2001a, *A&A*, 372, 820

- Bowen, D. V., Pettini, M., & Blades, J. C. 2002, *ApJ*, 580, 169
- Bowen, D. V., Tolstoy, E., Ferrara, A., Blades, J. C., & Brinks, E. 1997, *ApJ*, 478, 530
- Bowen, D. V., Tripp, T. M., & Jenkins, E. B., 2001b, *AJ*, 121, 1456
- Bresolin, F., Garnett, D. R., & Kennicutt, R. C. 2004, *ApJ*, in press (astro-ph/0407065)
- Bullock, J. S., Kravtsov, A. V., & Weinberg, D. H. 2000, *ApJ*, 539, 517
- Carignan, C. 1999, *PASA*, 16, 18
- Carignan, C., Beaulieu, S., Côté, S., Demers, S., & Mateo, M. *AJ*, 116, 1690
- Cen, R., & Ostriker, J. P. 1999, *ApJ*, 514, 1
- Cen, R., Ostriker, J. P., Prochaska, J. X., & Wolfe, A. M. 2003, *ApJ*, 598, 741
- Centurión, M., Molaro, P., Vladilo, G., Péroux, C., Levshakov, S. A., & D’Odorico, V. 2003, *A&A*, 403, 55
- Chen, H.-W., Lanzetta, K. M., Webb, J. K., & Barcons, X. 2001, *ApJ*, 559, 654
- Chen, H.-W., & Prochaska, J. X. 2000, *ApJ*, 543, L9
- Collins, J. A., Shull, J. M., & Giroux, M. L. 2003, *ApJ*, 585, 336
- Curran, S. J., Webb, J. K., Murphy, M. T. & Carswell, R. F. 2004, *MNRAS*, 351, L24
- Davé, R. et al. 2001, *ApJ*, 552, 473
- Davé, R., & Tripp, T. M. 2001, *ApJ*, 553, 528
- Davis, D. S., Mushotzky, R. F., Mulchaey, J. S., Worrall, D. M., Birkinshaw, M., & Burstein, D. 1995, *ApJ*, 444, 582
- Dessauges-Zavadsky, M., Péroux, C., Kim, T.-S., D’Odorico, S., & McMahon, R. G. 2003, *MNRAS*, 345, 447
- de Vaucouleurs, G. 1961, *ApJS*, 6, 213
- de Vaucouleurs, G., de Vaucouleurs, A., Corwin, J. R., Buta, R. J., Paturel, G., & Fouque, P. 1991, *Third Reference Catalog of Bright Galaxies* (New York: Springer)
- Ellison, S. L., Yan, L., Hook, I. M., Pettini, M., Wall, J. V., & Shaver, P. 2001, *A&A*, 379, 393
- Feldman, P. D., Sahnou, D. J., Kruk, J. W., Murphy, E. M., & Moos, H. W. 2001, *JGR*, 106, 8119
- Ferland, G. J., Korista, K. T., Verner, D. A., Ferguson, J. W., Kingdon, J. B., & Verner, E. M. 1998, *PASP*, 110, 761
- Field, G. B., & Steigman, G. 1971, 166, 59
- Fitzpatrick, E. L., & Spitzer, L. 1997, *ApJ*, 475, 623
- Fukugita, M., Hogan, C. J., & Peebles, P. J. E. 1998, *ApJ*, 503, 518
- Gibson, B. K., Giroux, M. L., Penton, S. V., Stocke, J. T., Shull, J. M., & Tumlinson, J. 2001, *AJ*, 122, 3280

- Giovanelli, R., & Haynes, M. P. 1989, *ApJ*, 346, L5
- Grebel, E. K., Gallagher, J. S., & Harbeck, D. 2003, *AJ*, 125, 1926
- Haardt, F., & Madau, P. 1996, *ApJ*, 461, 20
- Henry, R. B. C., Edmunds, M. G., & Köppen, J. 2000, *ApJ*, 541, 660
- Holweber, H. 2001, in *AIP Conf. Proc.* 598, *Solar and Galactic Composition*, ed. R. F. Wimmer-Schweingruber (New York: AIP), 23
- Howk, J. C., Prochaska, J. X., & Chen, H.-W. 2004, *ApJ*, submitted
- Howk, J. C., & Sembach, K. R. 1999, *ApJ*, 523, L141
- Impey, C. D., Petry, C. E., & Flint, K. P. 1999, *ApJ*, 524, 536
- Izotov, Y. I., Chaffee, F. H., Foltz, C. B., Green, R. F., Guseva, N. G., & Thuan, T. X. 1999, *ApJ*, 527, 757
- Jannuzi, B. T. et al. 1998, *ApJS*, 118, 1
- Jenkins, E. B. 1996, *ApJ*, 471, 292
- Jenkins, E. B. 2003, in *Carnegie Observatories Astrophysics Series, Vol. 4: Origin and Evolution of the Elements*, eds. A. McWilliam & M. Rauch 2003 (Cambridge: Cambridge University Press), in press (astro-ph/0309651)
- Jenkins, E. B., Bowen, D. V., Tripp, T. M., & Sembach, K. R. 2004, in preparation
- Jenkins, E. B., et al. 2000, *ApJ*, 538, L81
- Jenkins, E. B., & Tripp, T. M. 2001, *ApJS*, 137, 297
- Jenkins, E. B., Tripp, T. M., Wozniak, P. R., Sofia, U. J., & Sonneborn, G. 1999, *ApJ*, 520, 182
- Kepner, J., Tripp, T. M., Abel, T., & Spergel, D. 1999, *AJ*, 117, 2063
- Kimble, R. A., et al. 1998, *ApJ*, 492, L83
- Kim Quijano, J. et al. 2003, “STIS Instrument Handbook”, (Baltimore: STScI)
- Kobulnicky, H. A., & Kewley, L. J. 2004, *ApJ*, in press (astro-ph/0408128)
- Lauroesch, J. T., Truran, J. W., Welty, D. E., & York, D. G. 1996, *PASP*, 108, 641
- Lecavelier des Etangs, A., Désert, J. M., Kunth, D., Vidal-Madjar, A., Callejo, G., Ferlet, R., Hébrard, G., & Lebouteiller, V. 2004, *A&A*, 413, 131
- Lehner, N., Jenkins, E. B., Gry, C., Moos, H. W., Chayer, P., Lacour, S. 2003, *ApJ*, 595, 858
- Levshakov, S. A., Agafonova, I. I., Reimers, D., & Baade, R. 2003, *A&A*, 404, 449
- Lu, L., Sargent, W. L. W., Barlow, T. A., Churchill, C. W., & Vogt, S. 1996, *ApJS*, 107, 475
- Lockman, F. J., & Savage, B. D. 1995, *ApJS*, 97, 1
- Maller, A. H., Prochaska, J. X., Somerville, R. S., & Primack, J. R. 2003, 343, 268
- McWilliam, A. 1997, *ARA&A*, 35, 503

- Meyer, D. M., Cardelli, J. A., & Sofia, U. J. 1997, *ApJ*, 490, L103
- Meyer, D. M., Jura, M., & Cardelli, J. A. 1998, 493, 222
- Moos, H. W., et al. 2002, *ApJS*, 140, 3
- Morton, D. C. 1991, *ApJS*, 77, 119
- Morton, D. C., 1999, private communication to the FUSE Team
- Morton, D. C. & Dinerstein H. L. 1976, *ApJ*, 204, 1
- Murphy, E. M., et al. 2000, *ApJ*, 538, L35
- Nagamine, K., Springel, V., & Hernquist, L. 2004, *MNRAS*, 348, 435
- Péroux, C., Dessauges-Zavadsky, M., D’Odorico, S., Kim, T.-S., & McMahon, R. G. 2003, *MNRAS*, 345, 480
- Persic, M., & Salucci, P. 1992, *MNRAS*, 258, 14P
- Pettini, M., Ellison, S. L., Bergeron, J., & Petitjean, P. 2002, *A&A*, 391, 21
- Pettini, M., Ellison, S. L., Steidel, C. C., & Bowen, D. V. 1999, *ApJ*, 510, 576
- Pettini, M., Lipman, K., & Hunstead, R. W. 1995, *ApJ*, 451, 100
- Pettini, M., Madau, P., Bolte, M., Prochaska, J. X., Ellison, S. L., & Fan, X. 2003, *ApJ*, 594, 695
- Pilyugin, L. S., Thuan, T. X., & Vílchez, J. M. 2003, *A&A*, 397, 487
- Pisano, D. J., Wakker, B. P., Wilcots, E. M., & Fabian, D. 2004, *AJ*, 127, 199
- Prochaska, J. X. 2003, in *Carnegie Observatories Astrophysics Series, Vol. 4: Origin and Evolution of the Elements*, eds. A. McWilliam & M. Rauch 2003, in press (astro-ph/0310814)
- Prochaska, J. X., Gawiser, E., Wolfe, A. M., Castro, S., & Djorgovski, S. G. 2003, *ApJ*, 595, L9
- Prochaska, J. X., Henry, R. B. C., O’Meara, J. M., Tytler, D., Wolfe, A. M., Kirkman, D., Lubin, D., & Suzuki, N. 2002b, *PASP*, 114, 933
- Prochaska, J. X., Howk, J. C., O’Meara, J. M., Tytler, D., Wolfe, A. M., Kirkman, D., Lubin, D., & Suzuki, N. 2002a, *ApJ*, 571, 693
- Prochaska, J. X., & Wolfe, A. M. 2002, *ApJ*, 566, 68
- Putman, M. E., Staveley-Smith, L., Freeman, K. C., Gibson, B. K., & Barnes, D. G. 2003, *ApJ*, 586, 170
- Rao, S., & Turnshek, D. A. 2000, *ApJS*, 130, 1
- Richter, P., Savage, B. D., Tripp, T. M., & Sembach, K. R. 2004, *ApJS*, 153, 165
- Richter, P., Sembach, K. R., Wakker, B. P., Savage, B. D., Tripp, T. M., Murphy, E. B., Kalberla, P. M. W., & Jenkins, E. B. 2001, *ApJ*, 559, 318
- Rosenberg, J. L., Ganguly, R., Giroux, M. L., & Stocke, J. T. 2003, *ApJ*, 591, 677

- Salzer, J. J., di Serego Alighieri, S., Matteucci, F., Giovanelli, R., & Haynes, M. P. 1991, *AJ*, 101, 1258
- Savage, B. D., Bohlin, R. C., Drake, J. F., & Budich, W. 1977, *ApJ*, 216, 291
- Savage, B. D., & Sembach, K. R. 1991, *ApJ*, 379, 245
- Savage, B. D., & Sembach, K. R. 1996, *ARA&A*, 34, 279
- Savage, B. D., Sembach, K. R., Tripp, T. M., & Richter, P. 2002, *ApJ*, 564, 631
- Schaye, J. 2001, *ApJ*, 559, 507
- Schaye, J., Aguirre, A., Kim, T.-S., Theuns, T., Rauch, M., & Sargent, W. L. W. 2003, *ApJ*, 596, 768
- Schindler, S., Binggeli, B., & Böhringer, H. 1999, *A&A*, 343, 420
- Schneider, S. E. 1989, *ApJ*, 343, 94
- Sembach, K. R., Howk, J. C., Savage, B. D., Shull, J. M., & Oegerle, W. R. 2001, *ApJ*, 561, 573
- Sembach, K. R., & Savage, B. D. 1992, *ApJS*, 83, 147
- Sembach, K. R., Tripp, T. M., Savage, B. D., & Richter, P. 2004a, *ApJS*, in press (astro-ph/0407549)
- Sembach, K. R., Wakker, B. P., Tripp, T. M., et al. 2004b, *ApJS*, 150, 387
- Shetrone, M. D., Côté, P., & Sargent, W. L. W. 2001, *ApJ*, 548, 592
- Simcoe, R. A., Sargent, W. L. W., & Rauch, M. 2004, *ApJ*, 606, 92
- Shull, J. M., et al. 2000, *ApJ*, 538, L13
- Shull, J. M., Roberts, D., Giroux, M. L., Penton, S. V., & Fardal, M. A. 1999, *AJ*, 118, 1450
- Sofia, U. J., & Jenkins, E. B. 1998, *ApJ*, 499, 951
- Songaila, A. 2001, *ApJ*, 561, L153
- Sonneborn, G., Tripp, T. M., Ferlet, R., Jenkins, E. B., Sofia, U. J., Vidal-Madjar, A., & Wozniak, P. R. 2000, *ApJ*, 545, 277
- Spergel, D. N. et al. 2003, *ApJS*, 148, 175
- Tolstoy, E., Venn, K. A., Shetrone, M., Primas, F., Hill, V., Kaufer, A., & Szeifert, T. 2003, *AJ*, 125, 707
- Tripp, T. M., et al. 2002, *ApJ*, 575, 697
- Tripp, T. M., et al. 2003, *AJ*, 125, 3122
- Tripp, T. M., Giroux, M. L., Stocke, J. T., Tumlinson, J., & Oegerle, W. R. 2001, *ApJ*, 563, 724
- Tripp, T. M., Savage, B. D., & Jenkins, E. B. 2000a, *ApJ*, 534, L1
- Tripp, T. M., & Savage, B. D. 2000b, *ApJ*, 542, 42
- Tully, R. B., & Shaya, E. J. 1984, *ApJ*, 281, 31

- Tumlinson, J. et al. 2002, *ApJ*, 566, 857
- van Zee, L., Westpfahl, D., Haynes, M., & Salzer, J. 1998, *AJ*, 115, 1000
- Vila-Costas, M. B., & Edmunds, M. G. 1993, *MNRAS*, 265, 199
- Wakker, B. P. 2001, *ApJS*, 136, 463
- Wakker, B. P., et al. 2003, *ApJS*, 146, 1
- Wakker, B. P., & van Woerden, H. 1997, *ARA&A*, 35, 217
- Weymann, R. J., Vogel, S. N., Veilleux, S., & H. W. Epps 2001, *ApJ*, 561, 559
- Wolfe, A. M., Turnshek, D. A., Smith, H. E., & Cohen, R. D. 1986, *ApJS*, 61, 249
- Woodgate, B. E., et al. 1998, *PASP*, 110, 1183

Table 1. H I Column Densities: Virgo sub-DLA and Adjacent Lines

Observed Wavelength	Line Identification	z_{abs}	$\log N(\text{H I})$	Method ^a
1215.60	H I Ly α	0.0	20.17 \pm 0.03	1
1220.23	H I Ly α	0.00375	13.64 \pm 0.09	2
1223.34	H I Ly α	0.00632	19.32 \pm 0.03	1

^aColumn densities and uncertainties determined using the following methods: (1) fit to the Lorentzian wings of the damped Ly α profile as described in Jenkins et al. (1999), and (2) Voigt profile fit to the weak Ly α line.

Table 2. Metal Line Equivalent Widths and Integrated Column Densities

Species	λ_0^a (Å)	$\log f \lambda_0^a$	W_r (mÅ)	$\log N_a$
All Components ^b				
O I	1302.17	1.830	94.1±8.3	14.32±0.05
C II	1334.53	2.229	110.0±8.6	>13.96 ^c
Si II	1190.42	2.543	66.8±15.2	13.40 ^{+0.09c} _{-0.12}
	1260.42	3.174	140.0±7.8	>13.15 ^c
	1304.37	2.078	43.8±9.1	13.60±0.10
	1526.71	2.303	76.3±19.5	13.61 ^{+0.10} _{-0.13}
Strongest Component Only ^d				
O I	1302.17	1.830	75.5±5.5	14.21±0.05
N I	1199.55	2.193	(−23.5 ± 10.5)	<13.28
C II	1334.53	2.229	77.7±5.7	>13.84 ^c
Si II	1190.42	2.543	47.3±9.6	13.25 ^{+0.09c} _{-0.12}
	1260.42	3.174	98.2±5.1	> 13.03 ^c
	1304.37	2.078	26.2±6.2	13.40 ^{+0.09} _{-0.11}
	1526.71	2.303	53.5±12.9	13.45 ^{+0.10} _{-0.14}
Fe II	1608.45	1.970	16.7±5.2	13.23 ^{+0.12} _{-0.14}
C IV	1550.78 ^e	2.169	(8.3±15.4)	< 13.36
Si IV	1402.77 ^e	2.554	(−22.4±11.3)	< 12.88

^aRest-frame wavelength (λ_0) and oscillator strength (f) from Morton (1991) or Morton (1999).

^bRest-frame equivalent width [$W_r = W_{\text{ob}}/(1+z)$] and apparent column density integrated across the two main components of the absorber at $v = 0$ and 28 km s^{-1} .

^cThe column density from direct integration of this line is underestimated due to unresolved line saturation (see text, § 3).

^dEquivalent widths and column densities integrated over the velocity range of the strongest component only, i.e., the component at $v = 0 \text{ km s}^{-1}$ in Figure 3. Equivalent widths listed in parentheses have less than 3σ significance; these lines are not reliably detected, and we derive the 3σ upper limit on the column density from the equivalent width uncertainty assuming the linear curve of growth is applicable.

^eThe stronger C IV $\lambda 1548.20$ and Si IV $\lambda 1393.76$ lines cannot be measured due to blending with unrelated lines from other redshifts. Both lines of the N V $\lambda \lambda 1238.82, 1242.80$ doublet are blended, so no constraints can be placed on this species at this redshift.

Table 3. Component Velocities, Doppler Parameters, and Column Densities from Voigt-Profile Fitting

Species	Fitted Lines (Å)	v^a (km s ⁻¹)	b (km s ⁻¹)	log N
O I.....	1302.17	0±1	7±1	14.32±0.09
		28±2	9±3	13.66±0.09
C II.....	1334.53	-4±1	6±1	14.21±0.30
		28±1	8±2	13.36±0.08
Si II.....	1190.42, 1260.42, 1304.37, 1526.71	-2±1	6±1	13.44±0.06
		23±1	10±2	12.66±0.06
Fe II.....	1608.45	-4±1	3±1	13.43±0.11

^aVelocities in this table have been corrected for the wavelength calibration errors discussed in the appendix.

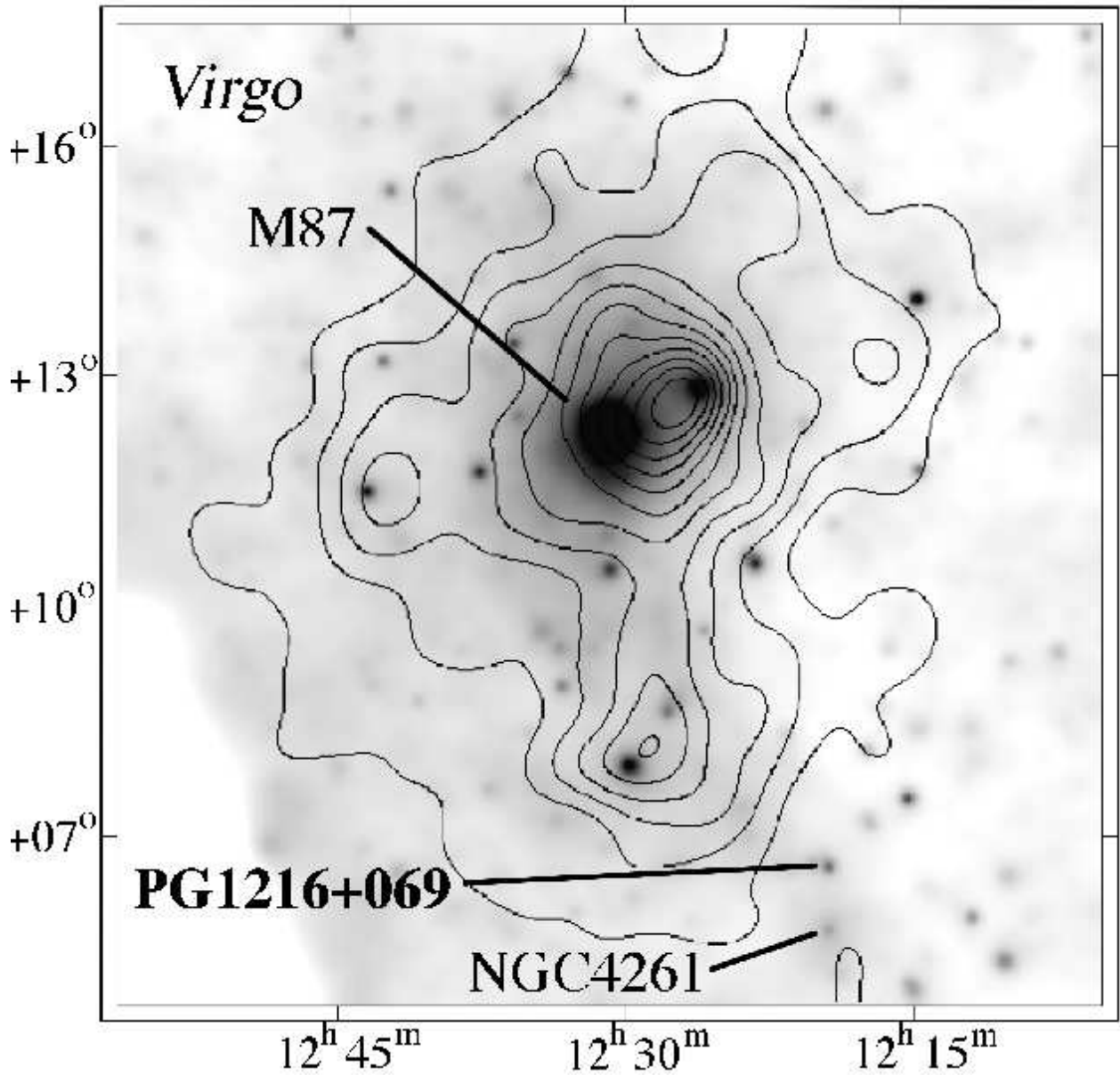


Fig. 1.— Location of the sight line to PG1216+069 plotted on the Schindler et al. (1999) map of X-ray emission in the vicinity of the Virgo cluster from the ROSAT all-sky survey (logarithmic grayscale; see also Böhringer et al. 1994) and galaxy number density from the VCC catalog (contours; see also Binggeli et al. 1993). The X-ray and galaxy number density maps have both been smoothed with a Gaussian with $\sigma = 24'$. The locations of M87 and the X-ray-bright NGC4261 group are also marked; see Davis et al. (1995) for a deeper, pointed ROSAT observation of the NGC4261 group.

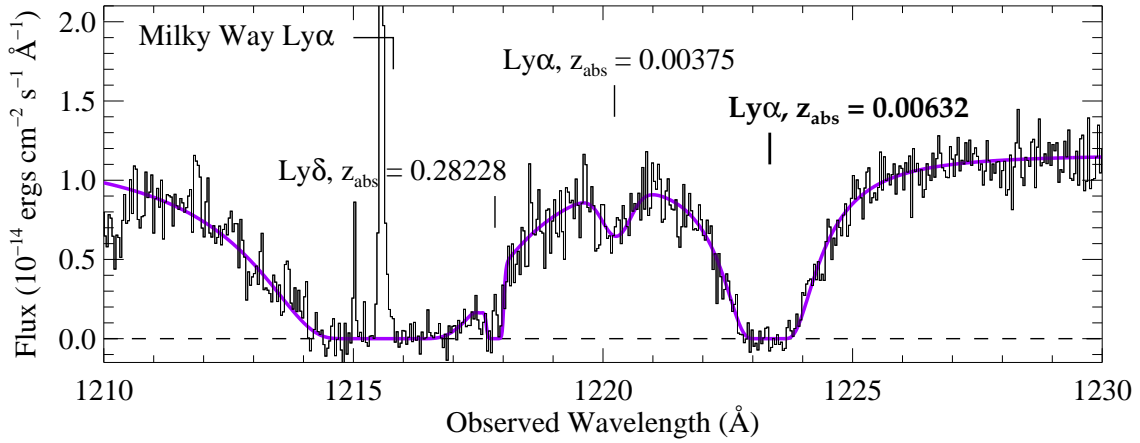


Fig. 2.— Region of the STIS E140M echelle spectrum of PG1216+069 showing the sub-damped Ly α absorber in the outskirts of the Virgo galaxy cluster at $z_{\text{abs}} = 0.00632$. The damped H I Ly α line due to the Milky Way ISM, a Ly α line at $z_{\text{abs}} = 0.00375$, and the Ly δ line at $z_{\text{abs}} = 0.28228$ are also marked. A fit to all of these features is overplotted with a thick line. The emission line in the core of the Milky Way Ly α profile is the geocoronal H I emission. At full (unbinned) resolution, the STIS E140M echelle mode provides 7 km s^{-1} resolution (FWHM) with ~ 2 pixels per resolution element. In this figure for display purposes only, the data have been binned 3 pixels into 1. For measurements and in all other figures, we use the full-resolution, unbinned STIS data.

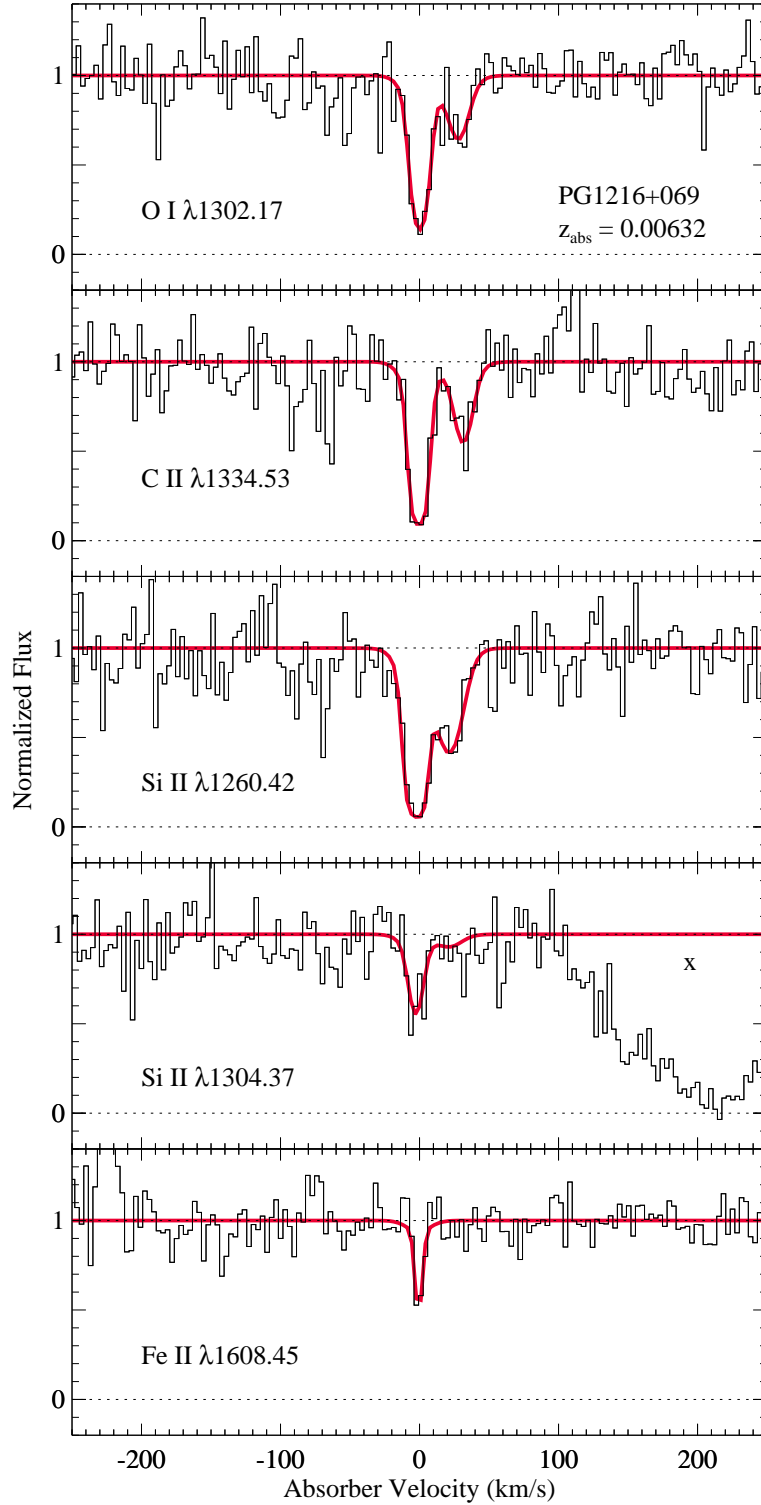


Fig. 3.— Continuum-normalized absorption profiles of lines detected in the sub-damped Ly α absorber at $z_{\text{abs}} = 0.00632$ (plotted vs. velocity in the absorber frame, i.e., $v = 0 \text{ km s}^{-1}$ at $z_{\text{abs}} = 0.00632$). The absorption-line fits summarized in Table 3 are overplotted with thick lines. An unrelated absorption feature in the Si II $\lambda 1304.37$ panel is marked with an 'x'.

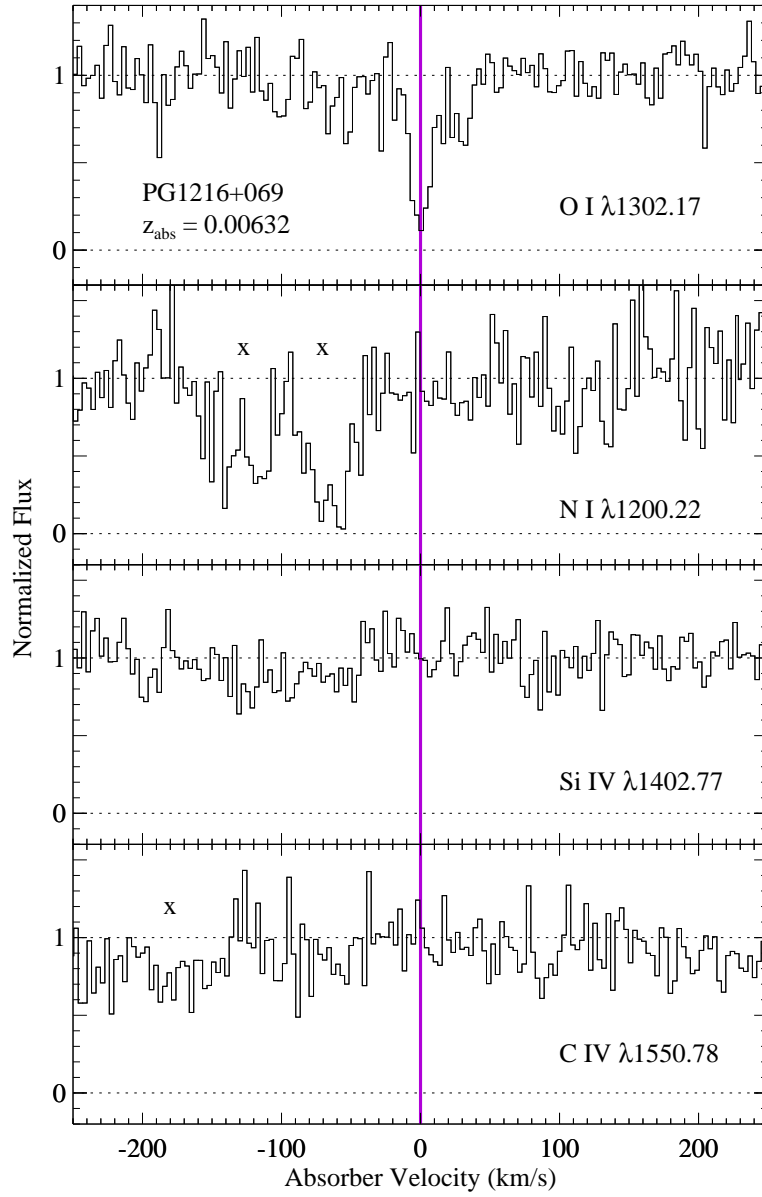


Fig. 4.— Continuum-normalized regions of lines that are *not* detected in the sub-damped Ly α absorber at $z_{\text{abs}} = 0.00632$ (lower three panels) with the O I $\lambda 1302.17$ profile replotted in the top panel for purposes of comparison. As in Figure 3, the data are plotted vs. velocity in the absorber frame where $v = 0 \text{ km s}^{-1}$ at $z_{\text{abs}} = 0.00632$. Unrelated absorption features from other redshifts are marked with an 'x'.

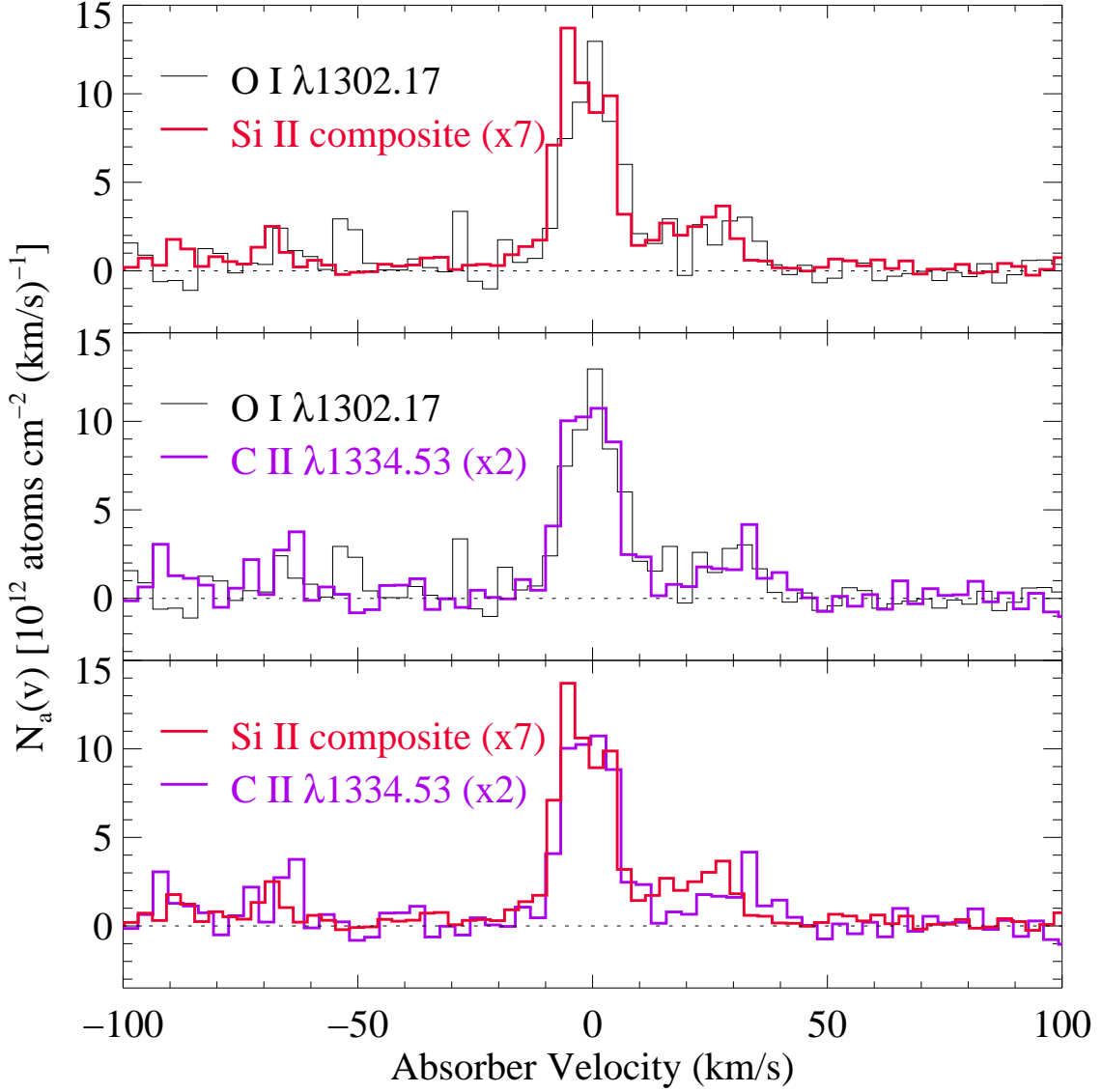


Fig. 5.— Comparison of apparent column density profiles, $N_a(v)$, of various species detected in the sub-DLA at $z_{\text{abs}} = 0.00632$: (top) O I $\lambda 1302.17$ (thin line) vs. a composite Si II profile (thick line) constructed from the Si II $\lambda\lambda 1190.42, 1260.42, 1304.37,$ and 1526.71 transitions (see text), (middle) O I $\lambda 1302.17$ (thin line) vs. C II $\lambda 1334.53$ (thick line), (bottom) Si II composite (thin line) vs. C II $\lambda 1334.53$ (thick line). In all panels, the Si II and C II profiles have been scaled up by factors of 7 and 2, respectively, and the velocities have been corrected as discussed in the appendix.

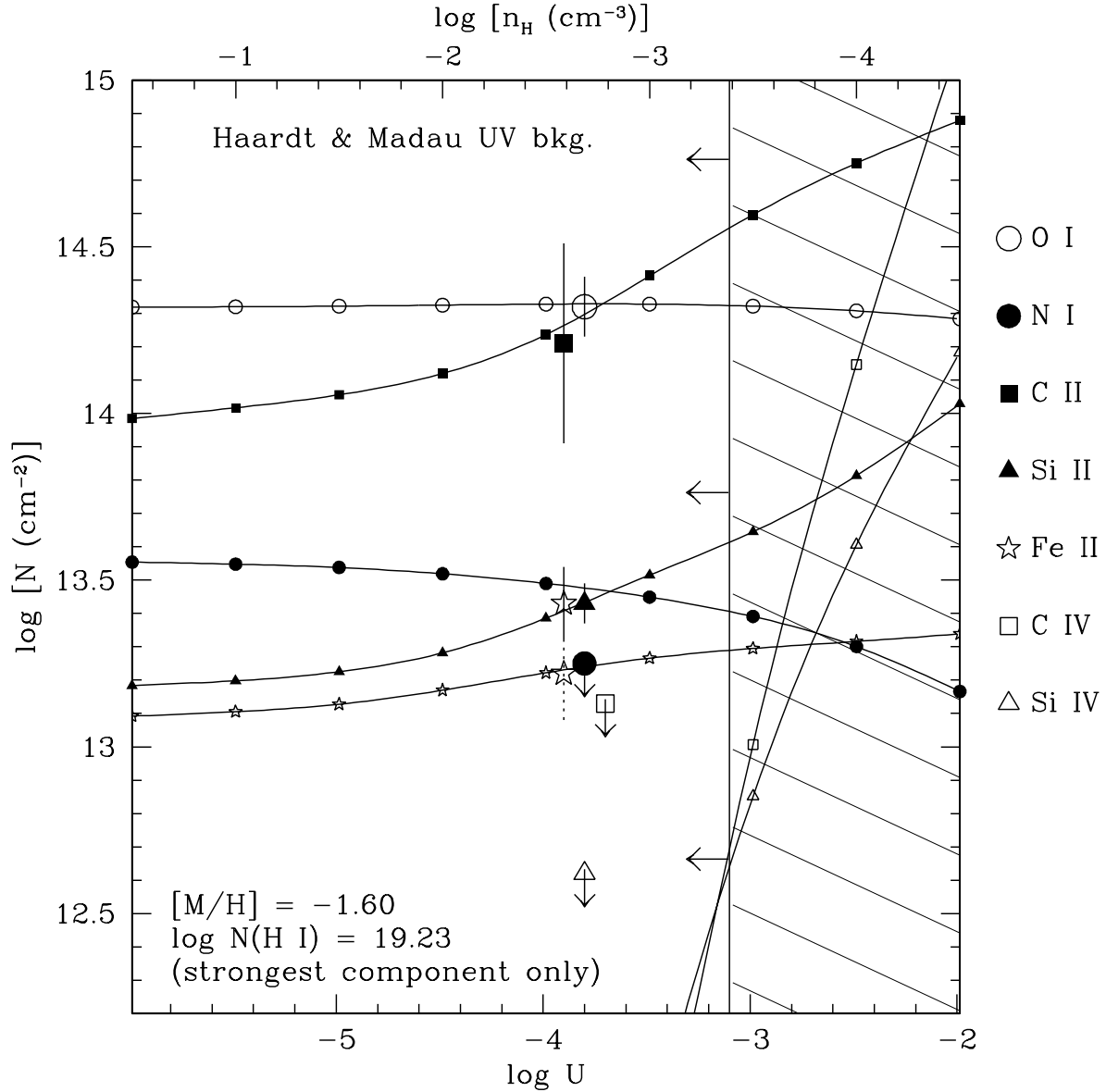


Fig. 6.— Comparison of column densities predicted by a photoionization model (solid curves with small symbols) to the observed columns in the stronger component of the sub-DLA at $z_{\text{abs}} = 0.00632$ (large symbols). The species corresponding to each symbol are shown in the key at right. The model column densities are plotted as a function of the ionization parameter U (lower axis, $U \equiv n_{\gamma}/n_{\text{H}}$) and the hydrogen number density (upper axis). The model assumes the Haardt & Madau (1996) UV background at $z = 0$ with $J_{\nu} = 1 \times 10^{-23}$ ergs cm^{-2} s^{-1} Hz^{-1} sr^{-1} . The observed column densities are plotted near the best-fitting value of $\log U \approx -3.8$, and points with arrows are 3σ upper limits from direct integration. For most of the well-detected species, we use the columns from component fitting in this plot. For iron, which is based on a single weak and narrow line, we show both the component-fitting measurement (upper point with solid error bars) and the column density from direct integration (lower point with dotted error bars). The model Si IV and C IV columns exceed the observed 3σ upper limits in the hatched portion of this figure; the Si IV constraint requires $\log U \leq -3.1$.

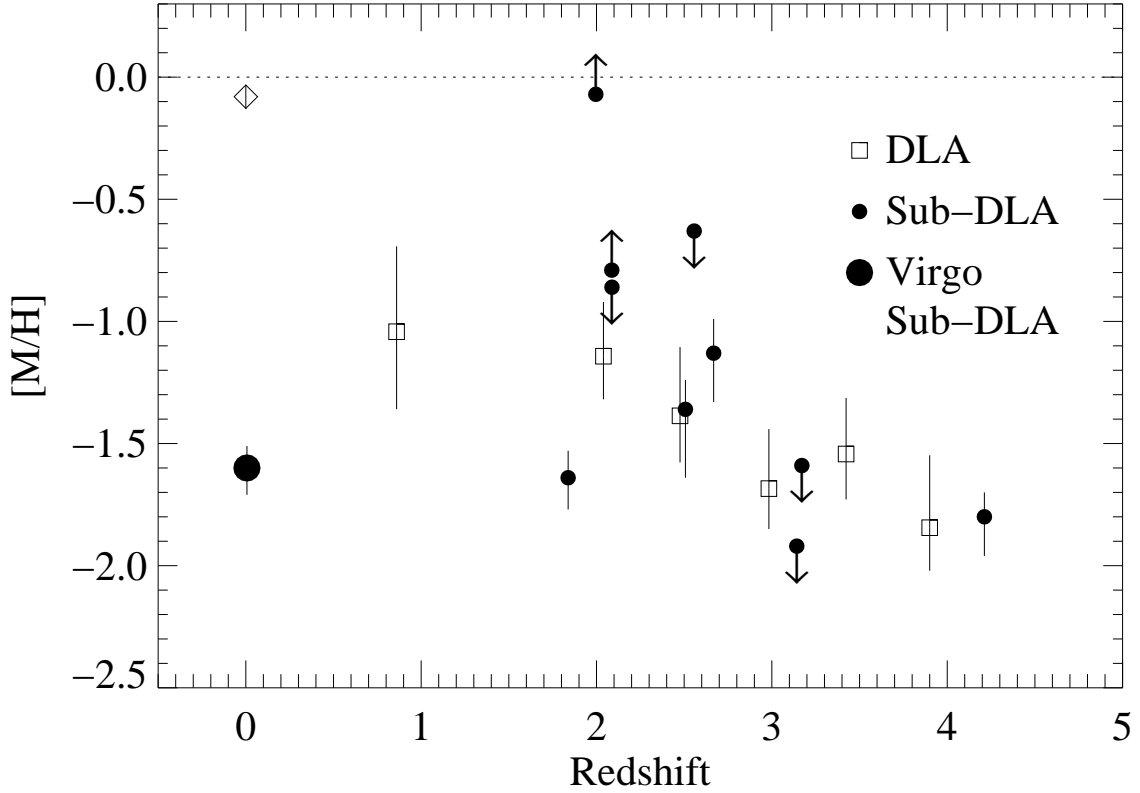


Fig. 7.— Logarithmic metallicity in the Virgo sub-DLA at $z_{\text{abs}} = 0.00632$ (large filled circle) compared to oxygen abundances in sub-DLAs at high redshifts (small filled circles) from the sample of Dessauges-Zavadsky et al. (2003) and the binned, unweighted mean metallicities from the sample of 125 DLAs (open squares) compiled by Prochaska et al. (2003). The DLA bins are shown with 95% confidence limits, and the bins at $z > 1.5$ contain equal numbers of DLA absorbers; the lowest-redshift bin contains fewer systems due to the paucity of low- z DLAs that have been found and measured. The diamond shows the mean oxygen abundance in the Milky Way ISM in the general vicinity of the Sun (Andre et al. 2003).

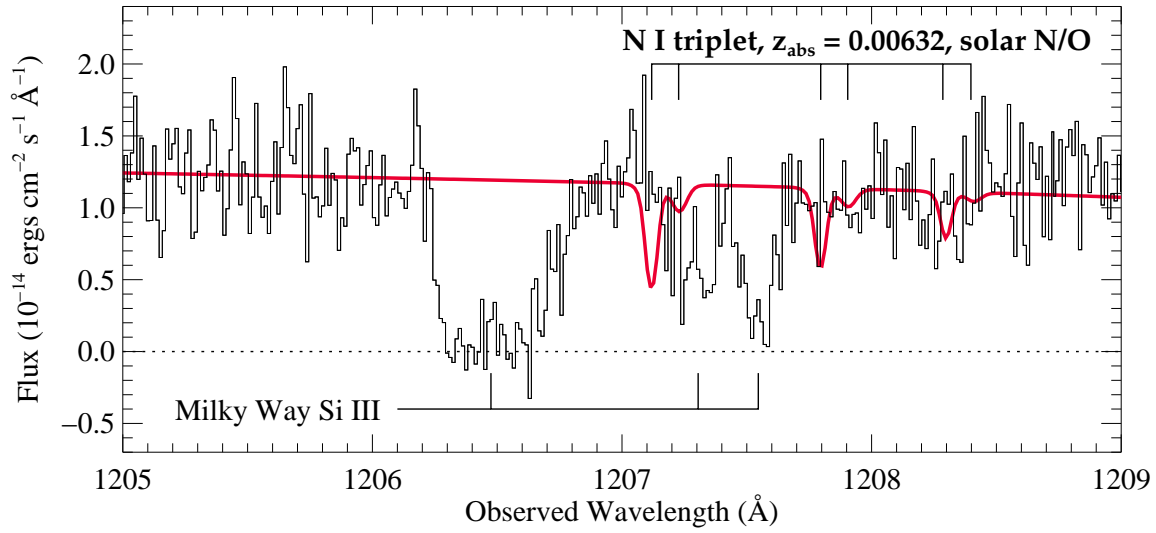


Fig. 8.— Comparison of the predicted absorption profiles of the N I $\lambda\lambda 1199.55, 1200.22, 1200.71$ triplet at $z_{\text{abs}} = 0.00632$, assuming the relative N/O abundance is solar, to the observed spectrum of PG1216+069. The N I triplet is redshifted into a noisy region of the spectrum, and moreover, it is blended with Si III $\lambda 1206.50$ absorption from high-velocity Milky Way gas. Nevertheless, the predicted N I profiles are clearly too strong; nitrogen is underabundant in this absorber.

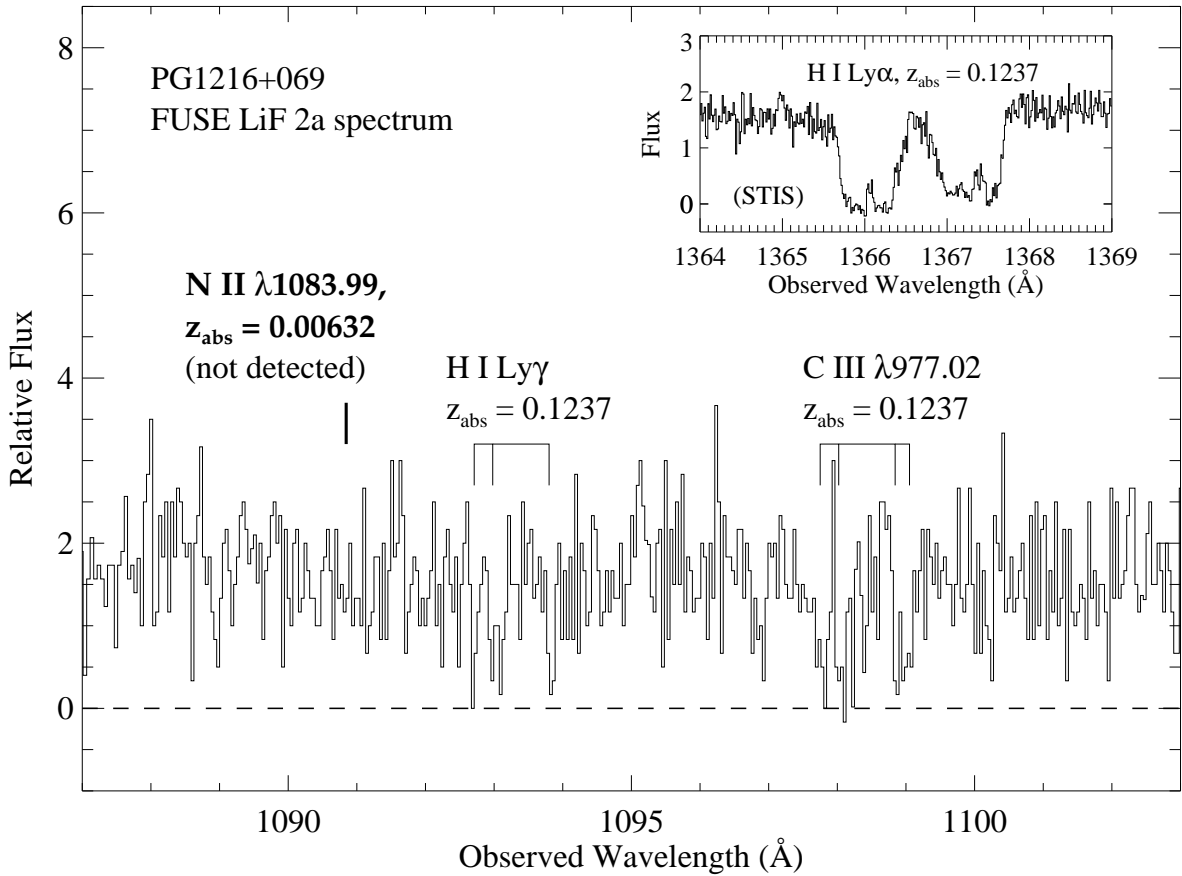


Fig. 9.— Portion of the *FUSE* spectrum of PG1216+069 covering the expected wavelength of the N II $\lambda 1083.99$ transition at $z_{\text{abs}} = 0.00632$. The spectrum is plotted vs. observed wavelength, and the redshifted wavelength of the N II line is indicated; no statistically significant feature is apparent at the expected position. The *FUSE* spectrum is relatively noisy, but nevertheless multiple Ly γ and C III $\lambda 977.02$ lines from the strong, multicomponent absorber at $z_{\text{abs}} = 0.1237$ are clearly detected; these lines are also marked. To corroborate the identification of these Ly γ and C III lines, the inset shows the multicomponent Ly α profile at $z_{\text{abs}} = 0.1237$ from the STIS spectrum; several of the components in the Ly α profile are also evident in the Ly γ and C III transitions. This figure shows only the LiF2a segment. The only other segment of the *FUSE* spectrum that covers this region (the SiC2b segment) is too noisy to provide any useful information.

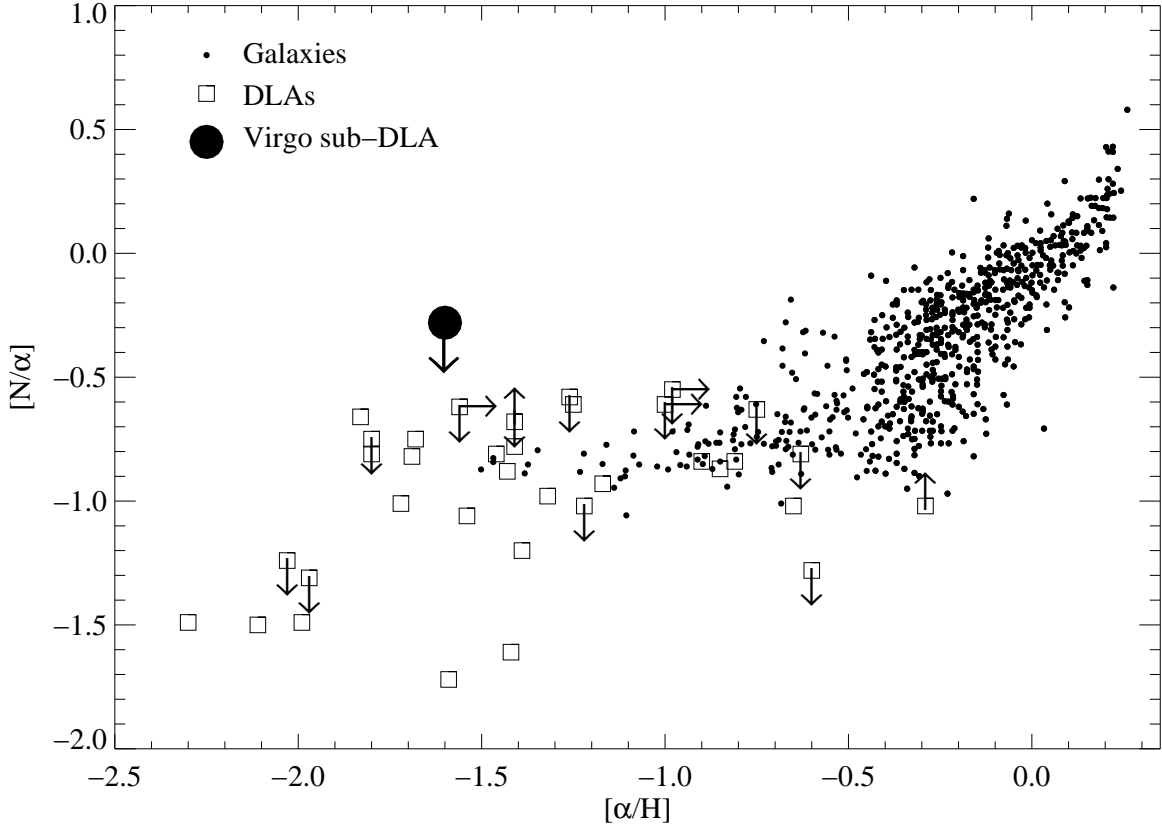


Fig. 10.— Nitrogen underabundance and absolute oxygen abundances measured in the PG1216+069 sub-DLA (large filled circle) compared to nitrogen abundance patterns observed in low-redshift galaxies (small filled circles) and high- z damped Ly α absorbers (open squares). The x-axis indicates the absolute α -element abundance, and the y-axis shows the relative nitrogen abundance with respect to an α -element. As discussed in § 4.1, oxygen provides the most reliable measurement of $[\alpha/H]$ and $[N/\alpha]$, so we prefer to use oxygen measurements when they are available. However, in some cases the oxygen lines are excessively saturated or not observed, in which case sulfur or silicon were used to estimate the α abundance. The galaxy H II region data were compiled by Pilyugin et al. (2003) and converted to abundances using the “P-method”. The high- z DLA measurements are from Centuri3n et al. (2003) with the exceptions and additions detailed by Jenkins et al. (2004).

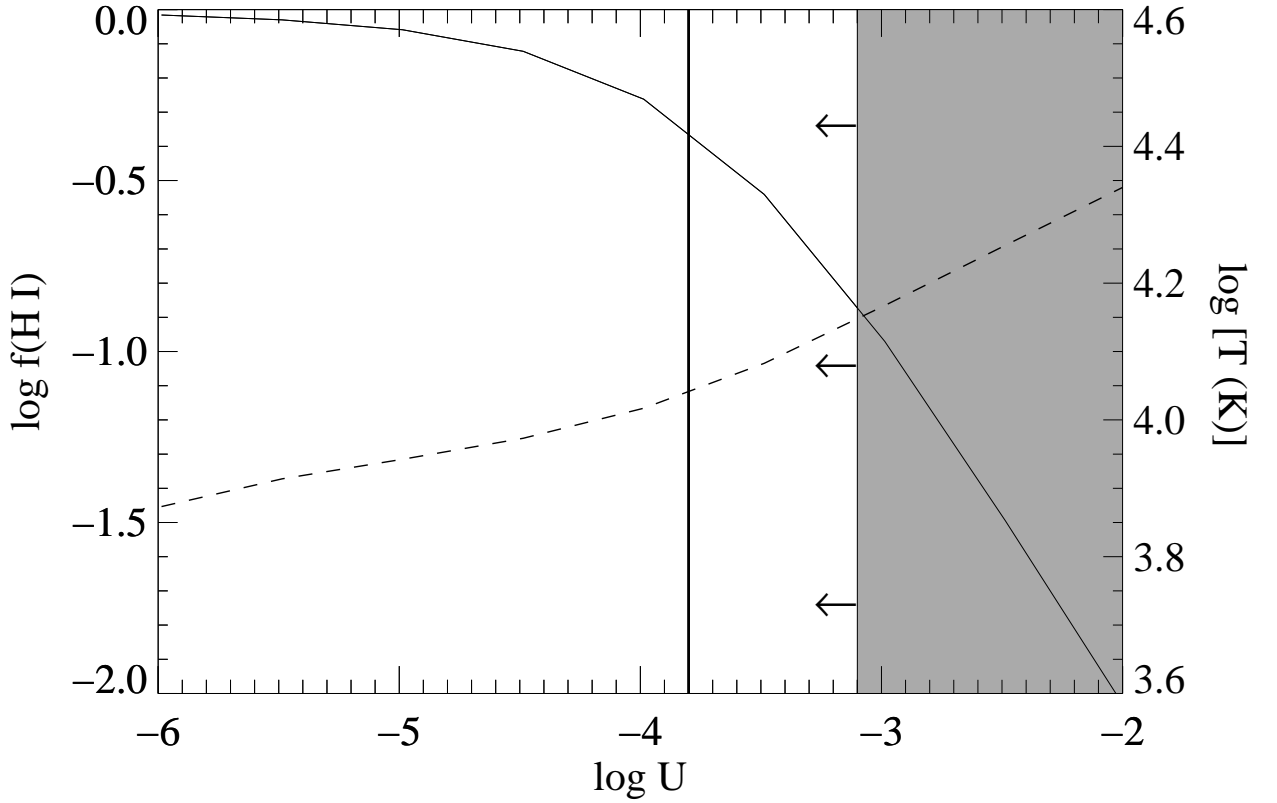


Fig. 11.— Neutral-gas content and mean temperature of the sub-DLA according to the photoionization model shown in Figure 6. The H I ion fraction is plotted with a solid line using the scale on the left axis, and the temperature is indicated with a dashed line using the scale on the right axis; both quantities are plotted vs. the ionization parameter U . The upper limits on C IV and Si IV require $\log U \lesssim -3.1$, as shown by the gray region. The thick vertical line is drawn at the value of U that provides the best fit to the observed column densities (see Figure 6).

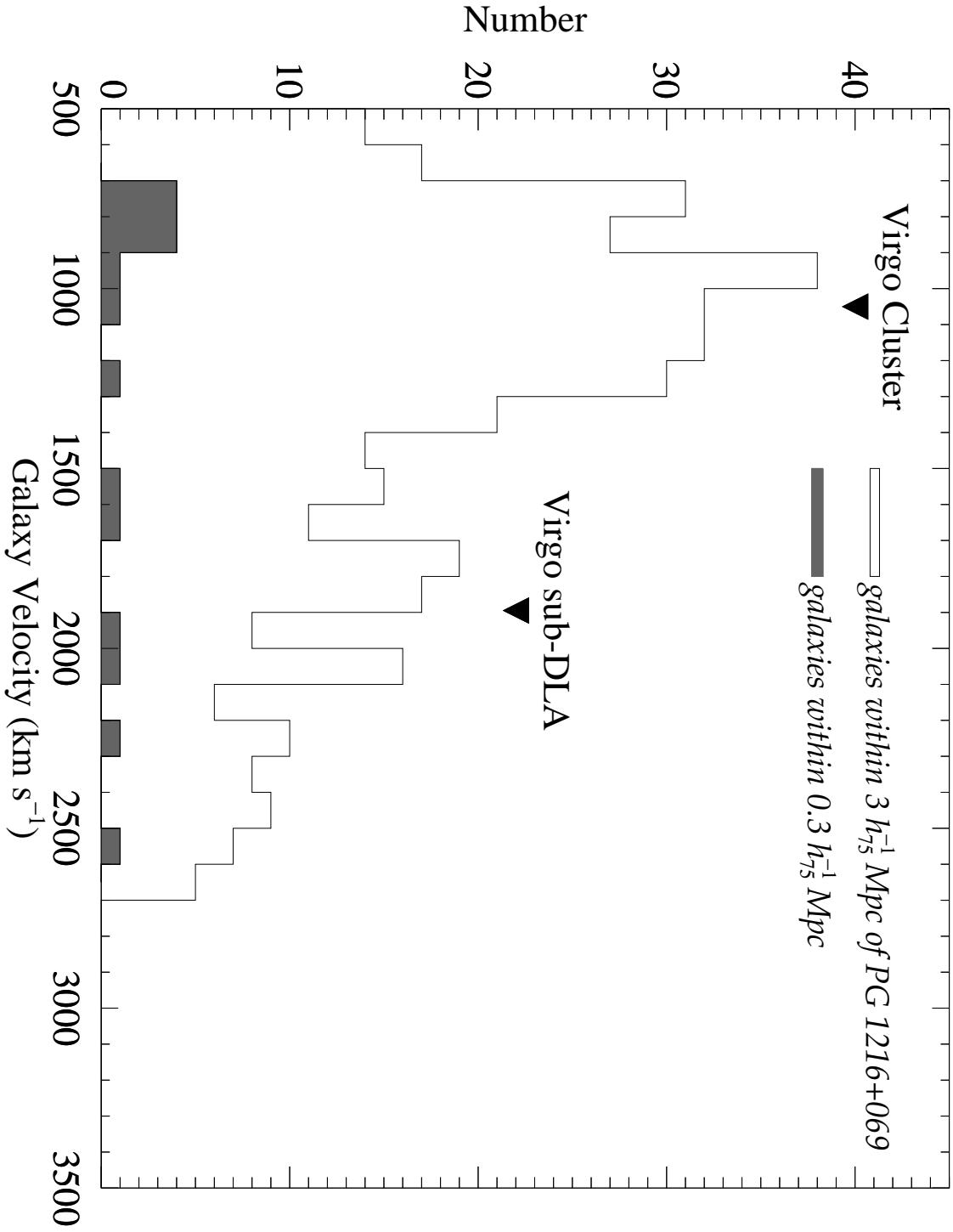


Fig. 12.— Number of RC3 galaxies within projected distances of $3h_{75}^{-1}$ Mpc (open histogram) and $300h_{75}^{-1}$ kpc (filled histogram) of the PG1216+069 sight line, plotted vs. redshift in 100 km s^{-1} bins. The redshift of the sub-DLA discussed in this paper is indicated.

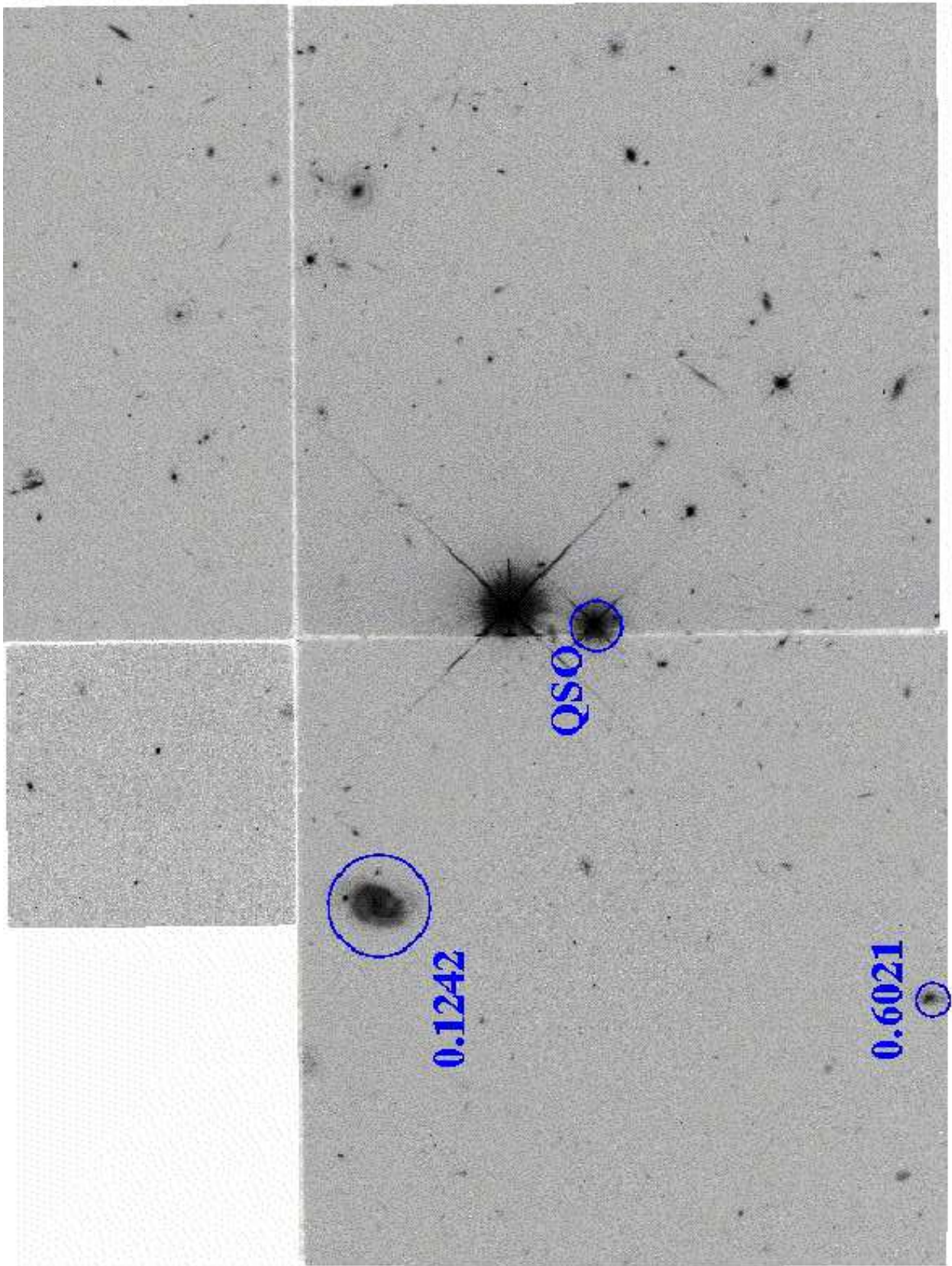


Fig. 13.— Portion of an image of the field surrounding PG1216+069 obtained with the WFPC2 camera on board *HST*. All galaxies within the image that have spectroscopically-measured redshifts

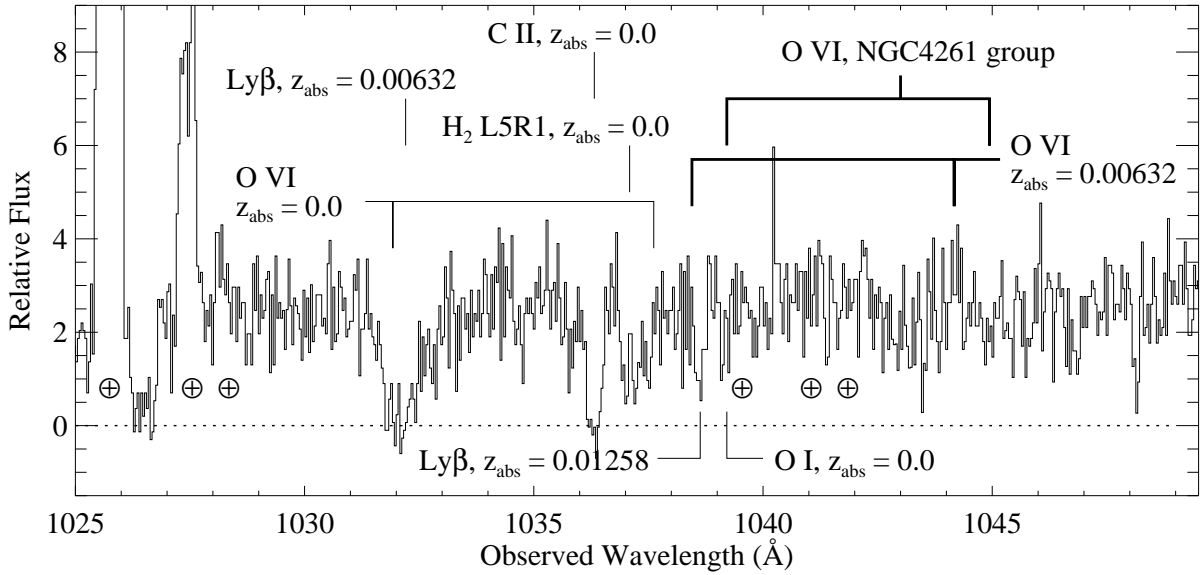


Fig. 14.— Portion of the *FUSE* spectrum covering the expected wavelengths of the O VI $\lambda\lambda 1031.93$, 1037.62 doublet at the redshift of the Virgo sub-DLA and the NGC4261 group. Well-detected absorption lines are labeled, and terrestrial airglow emission line wavelengths are also marked (\oplus). The stronger line of the O VI doublet at the Virgo/NGC4261 redshift falls in a region complicated by airglow emission, Galactic O I $\lambda 1039.23$ absorption (which appears to be filled in by airglow emission), and Lyman β absorption from $z_{\text{abs}} = 0.01258$. No significant absorption is evident at the wavelength of the weaker O VI line at Virgo redshifts.

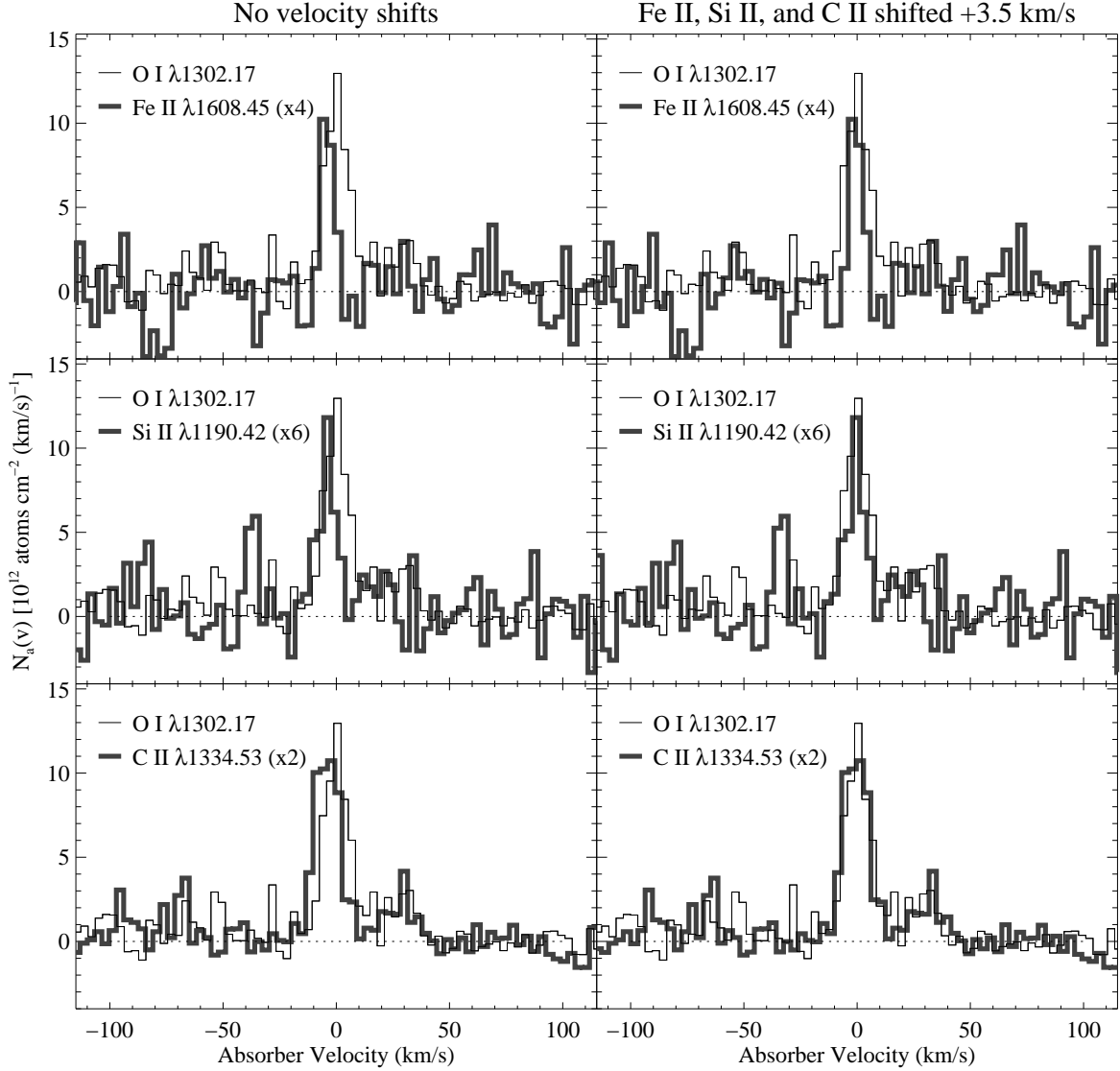


Fig. 15.— Comparison of the apparent column density profile of O I $\lambda 1302.17$ to the $N_a(v)$ profiles of Fe II $\lambda 1608.45$ (top), Si II $\lambda 1190.42$ (middle), and C II $\lambda 1334.53$ (bottom). The left panels show the $N_a(v)$ profiles with no shifts applied to the velocity scale; significant differences are evident in the centroids of the various lines. The right panels show the same comparisons, but with the Fe II, Si II, and C II profiles shifted by $+3.5 \text{ km s}^{-1}$, or roughly one pixel. For purposes of comparison, the Fe II, Si II, and C II $N_a(v)$ profiles have been scaled up by factors of 4, 6, and 2, respectively.

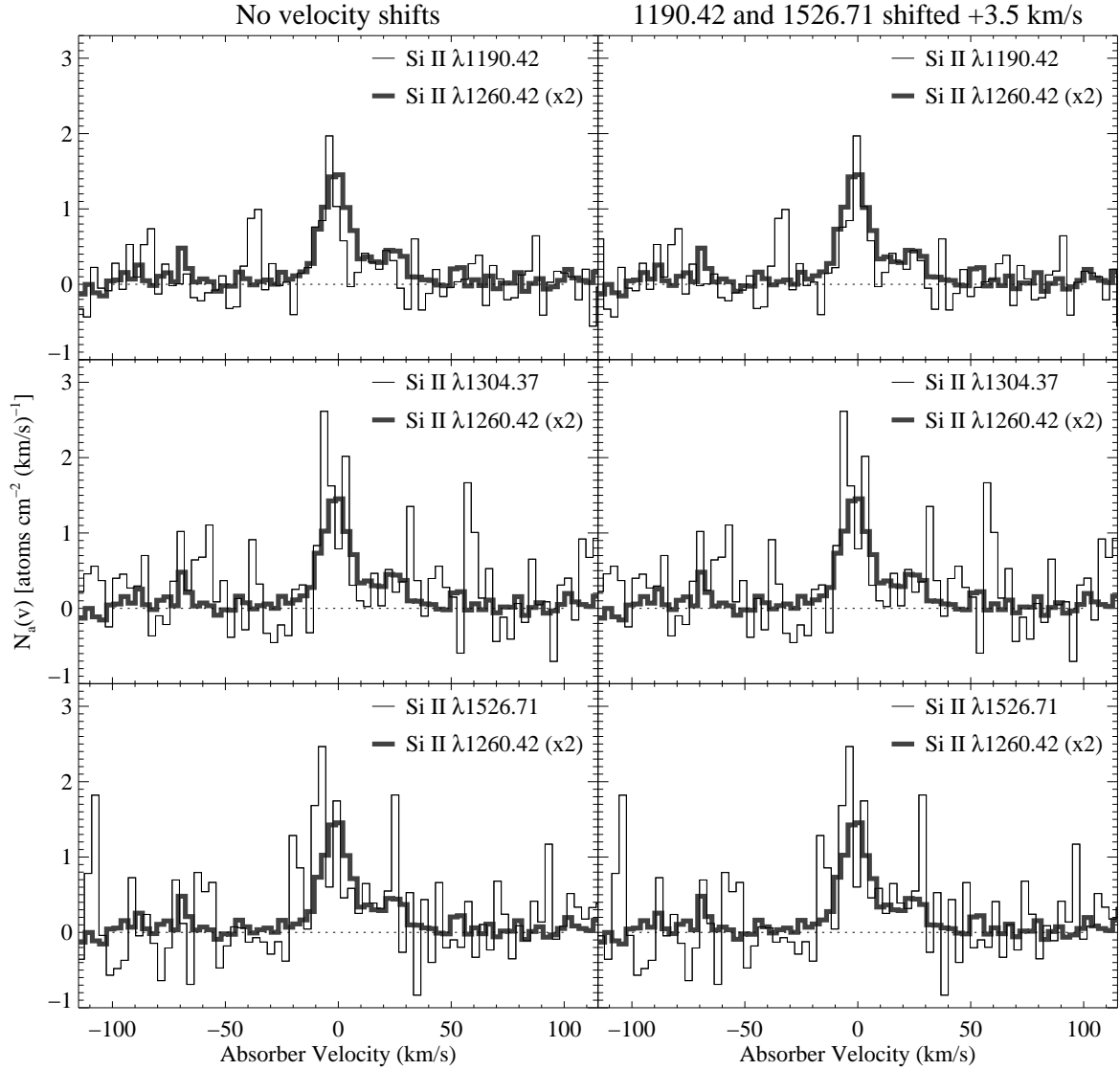


Fig. 16.— Comparison of the apparent column density profile of Si II λ 1260.42 to the $N_a(v)$ profiles of Si II λ 1190.42 (top), Si II λ 1304.37 (middle), and Si II λ 1526.71 (bottom). As in Figure 15, the left panels show the $N_a(v)$ profiles with no shifts applied to the velocity scale. The $N_a(v)$ profiles in this figure are somewhat noisier than the profiles shown in Figure 15, but nevertheless, close inspection reveals differences in the profile centroids. The right panels show the same comparisons, but with the 1190.42 and 1526.71 Å transitions shifted by $+3.5 \text{ km s}^{-1}$, which appears to provide better alignment of these lines.

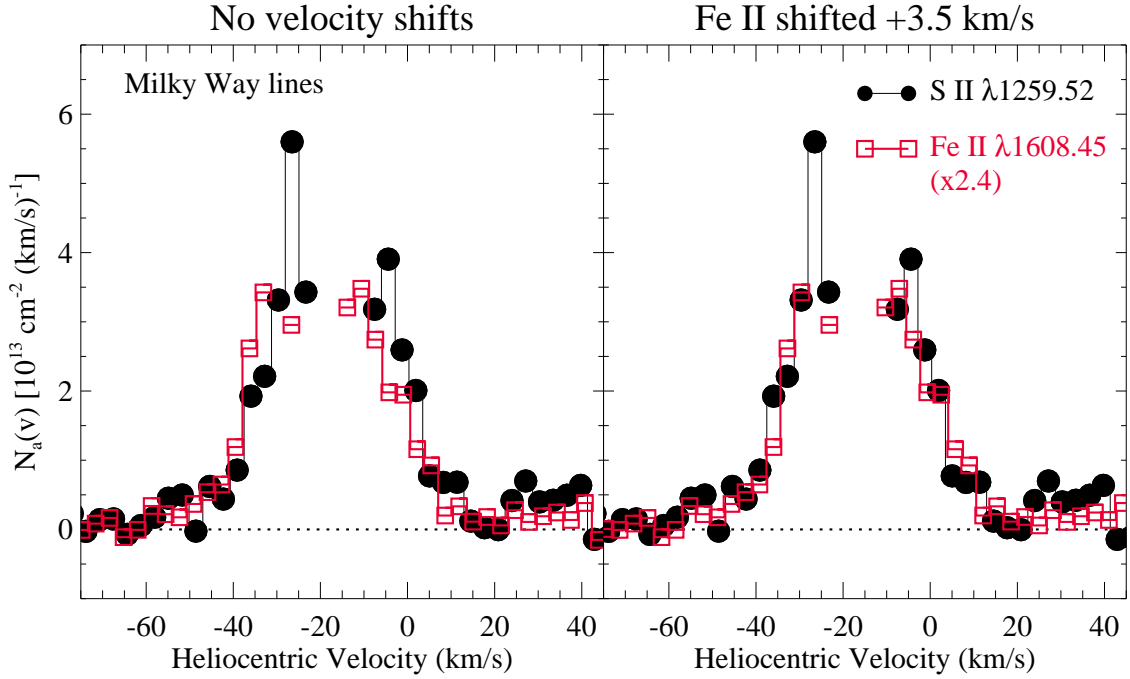


Fig. 17.— The $N_a(v)$ profile of the Milky Way S II $\lambda 1259.52$ transition (filled circles) vs. $N_a(v)$ of the Milky Way Fe II $\lambda 1608.45$ line (open squares). In the left panel, no shift has been applied to the wavelength scale, but in the right panel the Fe II line has been shifted by $+3.5 \text{ km s}^{-1}$. The profiles are not plotted in the line cores where both the S II and Fe II lines are saturated. These lines, which have nothing to do with the transitions from the $z_{\text{abs}} = 0.00632$ absorber shown in Figures 15 - 16, also indicate that a ~ 1 pixel correction is required for the wavelength scale of the Fe II line.